NASA/TP—2000–209905

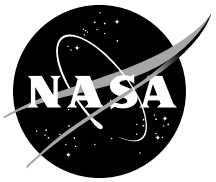

Modeling of Nonacoustic Combustion Instability in Simulations of Hybrid Motor Tests

M. Rocker
Marshall Space Flight Center, Marshall Space Flight Center, Alabama

February 2000

The NASA STI Program Office…in Profile

Since its founding, NASA has been dedicated to the advancement of aeronautics and space science. The NASA Scientific and Technical Information (STI) Program Office plays a key part in helping NASA maintain this important role.

The NASA STI Program Office is operated by Langley Research Center, the lead center for NASA's scientific and technical information. The NASA STI Program Office provides access to the NASA STI Database, the largest collection of aeronautical and space science STI in the world. The Program Office is also NASA's institutional mechanism for disseminating the results of its research and development activities. These results are published by NASA in the NASA STI Report Series, which includes the following report types:

- TECHNICAL PUBLICATION. Reports of completed research or a major significant phase of research that present the results of NASA programs and include extensive data or theoretical analysis. Includes compilations of significant scientific and technical data and information deemed to be of continuing reference value. NASA's counterpart of peer-reviewed formal professional papers but has less stringent limitations on manuscript length and extent of graphic presentations.

- TECHNICAL MEMORANDUM. Scientific and technical findings that are preliminary or of specialized interest, e.g., quick release reports, working papers, and bibliographies that contain minimal annotation. Does not contain extensive analysis.

- CONTRACTOR REPORT. Scientific and technical findings by NASA-sponsored contractors and grantees.

- CONFERENCE PUBLICATION. Collected papers from scientific and technical conferences, symposia, seminars, or other meetings sponsored or cosponsored by NASA.

- SPECIAL PUBLICATION. Scientific, technical, or historical information from NASA programs, projects, and mission, often concerned with subjects having substantial public interest.

- TECHNICAL TRANSLATION. English-language translations of foreign scientific and technical material pertinent to NASA's mission.

Specialized services that complement the STI Program Office's diverse offerings include creating custom thesauri, building customized databases, organizing and publishing research results…even providing videos.

For more information about the NASA STI Program Office, see the following:

- Access the NASA STI Program Home Page at ***http://www.sti.nasa.gov***

- E-mail your question via the Internet to help@sti.nasa.gov

- Fax your question to the NASA Access Help Desk at (301) 621–0134

- Telephone the NASA Access Help Desk at (301) 621–0390

- Write to:
  NASA Access Help Desk
  NASA Center for AeroSpace Information
  7121 Standard Drive
  Hanover, MD 21076–1320

NASA/TP—2000–209905

Modeling of Nonacoustic Combustion Instability in Simulations of Hybrid Motor Tests

M. Rocker
Marshall Space Flight Center, Marshall Space Flight Center, Alabama

National Aeronautics and
Space Administration

Marshall Space Flight Center • MSFC, Alabama 35812

February 2000

Acknowledgments

The author wishes to thank Terry A. Boardman and Ronn L. Carpenter, both of Thiokol and Charles F. Schafer of NASA Marshall Space Flight Center (MSFC) for challenging the author with this project. The author thanks Steven R. Wassom of Thiokol and Dan Mitchell of Marshall Space Flight Center for their efforts in acquainting the author with the Matrix-x software. The author thanks Scott E. Claflin of Boeing/Rocketdyne for the injector design drawings. Also, the author thanks Terry Able of Lockheed-Martin for the HPTLVB photographs. Finally, the author wishes to thank SCSC's Technical Illustrations and Publications Office for editing of this report.

TABLE OF CONTENTS

LIST OF FIGURES

LIST OF FIGURES (Continued)

LIST OF FIGURES (Continued)

LIST OF TABLES

LIST OF ACRONYMS

GN_2	gaseous nitrogen
gox	gaseous oxygen
HPDP	Hybrid Propulsion Development Program
HPTLVB	Hybrid Propulsion Technology for Launch Vehicle Boosters
HTPB	hydroxyl terminated polybutadiene
IR&D	independent research and development
JIRAD	joint industry research and development
lox	liquid oxygen
LSSRCS	large subscale solid rocket combustion simulator
MSFC	Marshall Space Flight Center
TEP	Thermochemical Equilibrium Program

TECHNICAL PUBLICATION

MODELING OF NONACOUSTIC COMBUSTION INSTABILITY IN SIMULATIONS OF HYBRID MOTOR TESTS

1. INTRODUCTION

Nonacoustic combustion instabilities are high-amplitude chamber pressure oscillations that have frequencies too low to be characterized as acoustic in nature. In hybrid motors, combustion instability of any frequency range may be initiated by one, or all, of four mechanisms:[1]

- Poor atomization from the injector in the head-end vaporization chamber
- Chuffing of the solid fuel in the ports
- Pressure-sensitivity of the combustion process, also in the fuel ports
- Flow-induced oscillations caused by vortex shedding in the aft mixing chamber.

A fifth mechanism of nonacoustic combustion instability, not intrinsic to the hybrid motor, is the hydrodynamic feedsystem coupling between the hybrid motor and liquid oxygen (lox) feedsystem.

A series of 17 subscale hybrid motor tests was conducted by Thiokol, Rocketdyne, and Martin Marietta at test stand 500 at NASA Marshall Space Flight Center (MSFC) in Huntsville, Alabama. Figures 1 and 2 illustrate the hybrid motor during pretest preparation and during hot-fire testing. These tests were conducted for the Hybrid Propulsion Technology for Launch Vehicle Boosters (HPTLVB) program,[2] funded under contract NAS8–39942. The test objective was to investigate the effects of oxidizer precombustion and oxidizer distribution on the combustion stability of hybrid motors. The mainstage duration of these tests was ≈10 sec. During some of these tests, nonacoustic combustion instabilities were observed.

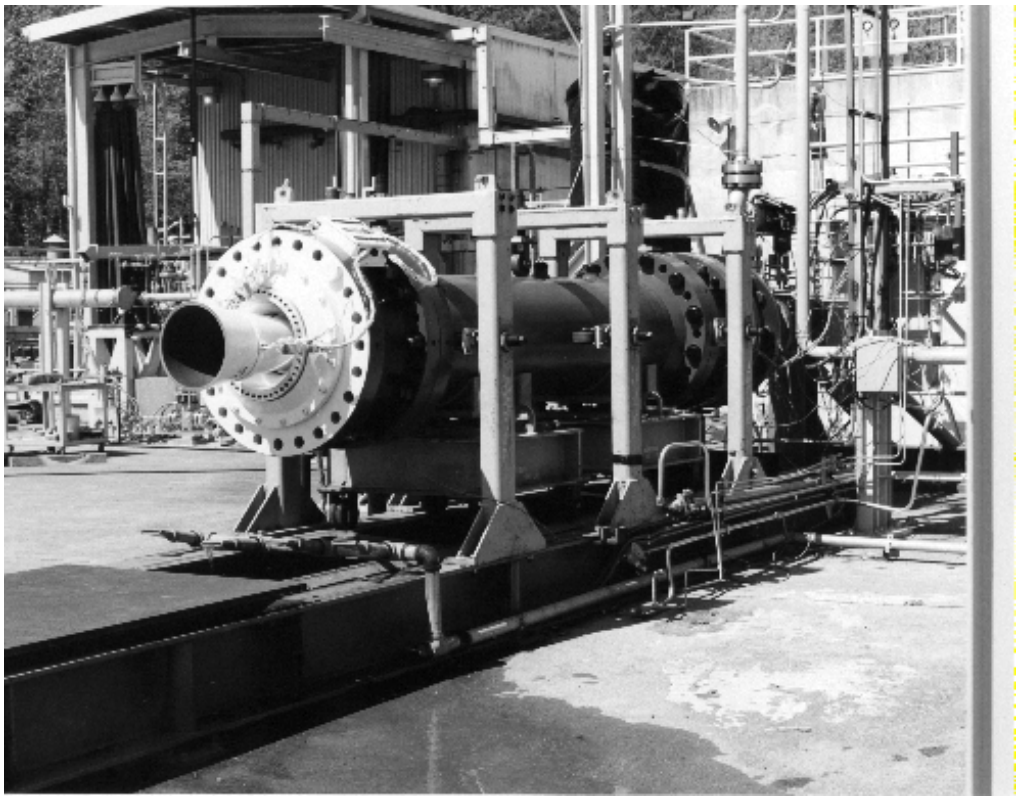

Figure 1. Twenty-four-in. hybrid motor prior to testing.

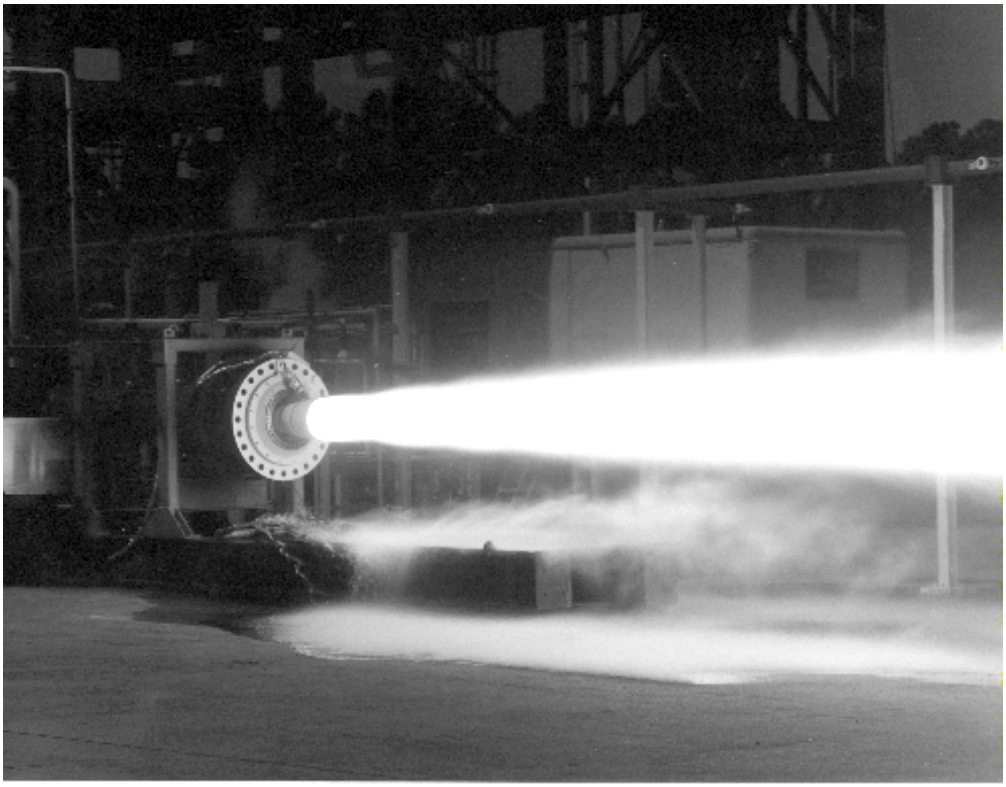

Figure 2. Twenty-four-in. hybrid motor during hot-fire testing.

2. DESCRIPTION OF THE HYBRID TEST SYSTEM

The test system consisted of the hybrid motor and lox feedsystem.

Figure 3 presents a sketch of the hybrid motor. The hybrid motor had a case diameter of 24 in. The vaporization chamber was at the head end of the hybrid motor and was lined with solid fuel that vaporized the lox when burned. The vaporization chamber had optional solid fuel fins. These fins extended radially from the walls to the center of the chamber and enhanced lox vaporization. The lox injector was within the vaporization chamber.

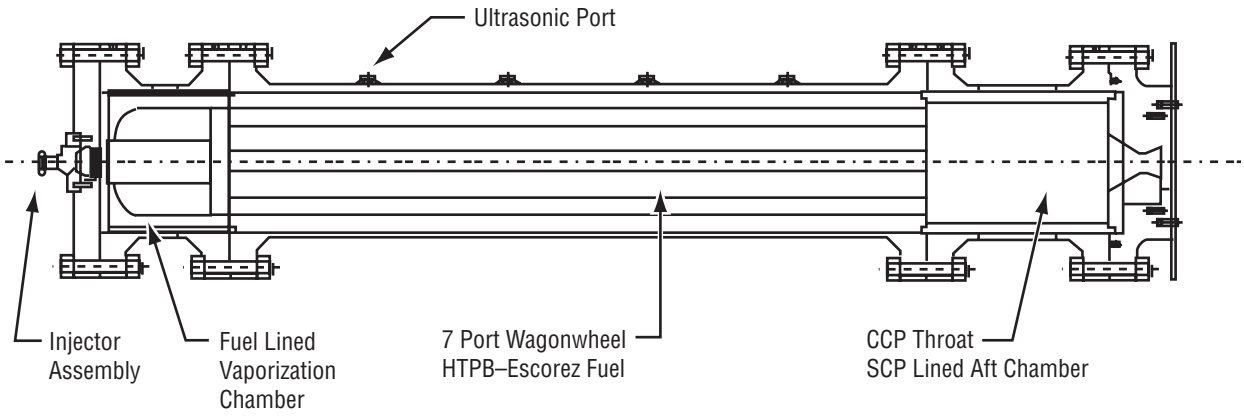

Figure 3. Twenty-four-in. hybrid motor.

Two injectors were used in the test series. The first injector was used in the large subscale solid rocket combustion simulator (LSSRCS) test series. The second injector was used in the joint industry research and development (JIRAD) test series. Both injector designs will be presented later. The solid fuel grain was downstream of the vaporization chamber. It was 108 in. long and consisted of hydroxyl terminated polybutadiene (HTPB)-based fuel. The solid fuel grain had six outer ports and a center port arranged in a wagon-wheel cross section. The mixing chamber was downstream of the solid fuel grain and the nozzle was downstream of the mixing chamber.

Figure 4 presents the lox feedsystem schematic. The lox feedsystem consisted of a 3,000-gal lox tank, cavitating venturi, valve, and lox injector, respectively. A total of 255 ft of 3-in.-diameter feedline connected these components.

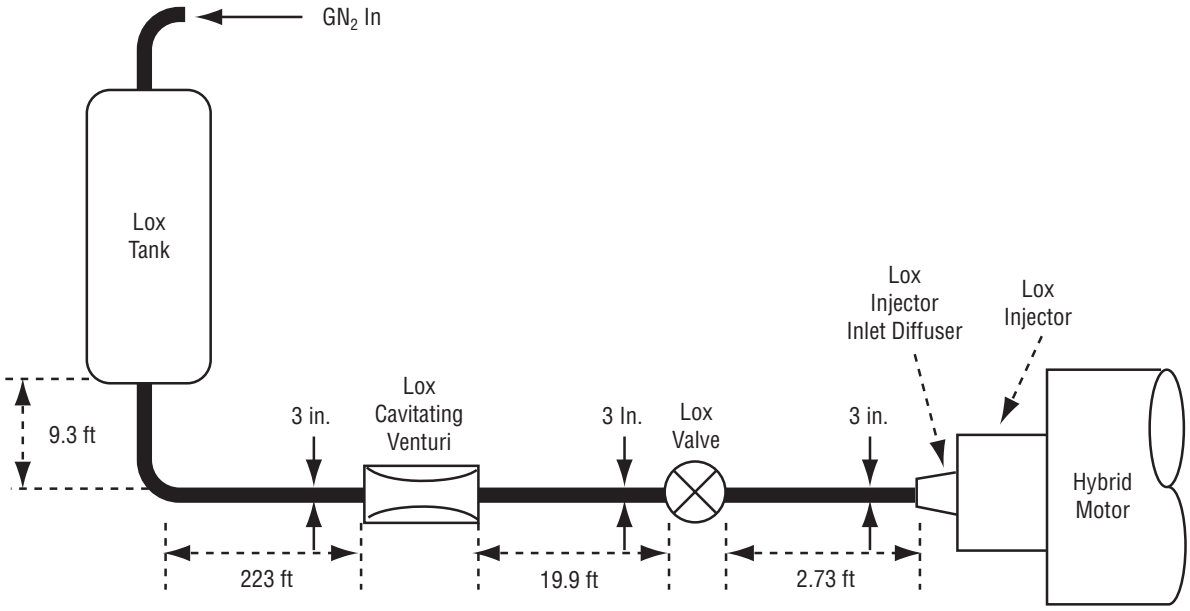

Figure 4. Lox feed system for the 24-in. hybrid motor tests.

3. TEST RESULTS

The following paragraphs present results of the first seven tests.

For test 1, the motor was tested with the LSSRCS injector, without the solid fuel fins in the vaporization chamber. The lox flow rate was 10 lbm/sec with an injector pressure drop of ≈44 percent of chamber pressure. Figure 5 presents the chamber pressure for test 1. A chamber pressure of 470 psi was achieved. The test was stable with no oscillations in the chamber pressure.

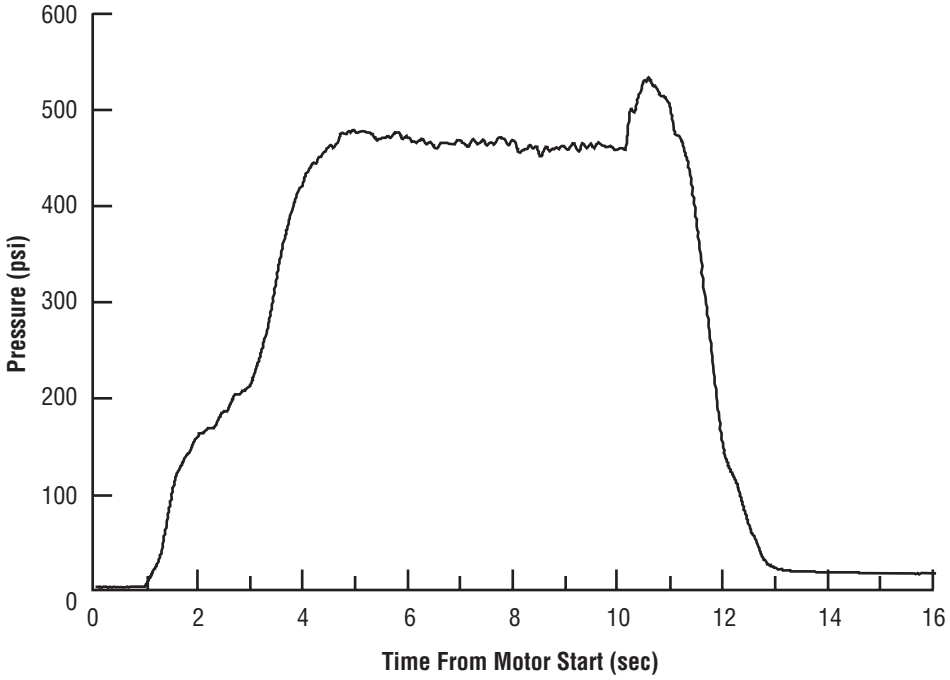

Figure 5. Test 1 chamber pressure.

For test 2, the motor was tested unaltered from test 1 with the exception of the injector. The test was performed with the JIRAD injector. The lox flow rate was 20 lbm/sec with an injector pressure drop of 11 percent of chamber pressure. Figure 6 presents chamber pressure for test 2. A chamber pressure of 440 psi was achieved. Unlike test 1, test 2 was unstable with large-amplitude, 6.5-Hz oscillations in chamber pressure that decayed just before the end of the test. The maximum amplitude of the oscillations was ≈20 percent (peak to peak) of chamber pressure.

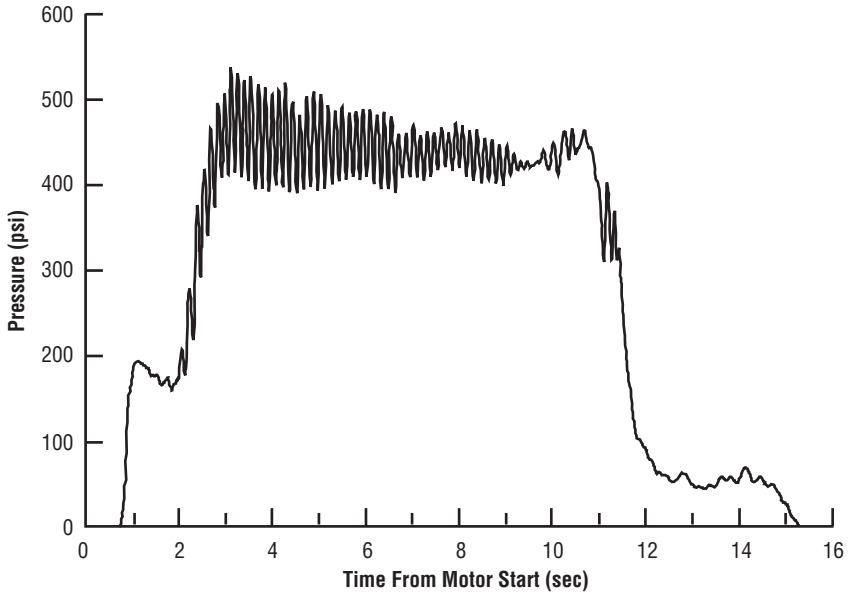

Figure 6. Test 2 chamber pressure.

For test 3, the motor was tested with a new solid fuel grain, solid fuel fins in the vaporization chamber, and the JIRAD injector. The lox flow rate was 20 lbm/sec with an injector pressure drop of 14 percent of chamber pressure. Figure 7 presents chamber pressure for test 3. A chamber pressure of 420 psi was achieved. Test 3 was unstable with large-amplitude, 7.5-Hz oscillations in chamber pressure that were sustained throughout the test. The amplitude of the oscillations was ≈25 percent (peak to peak) of chamber pressure.

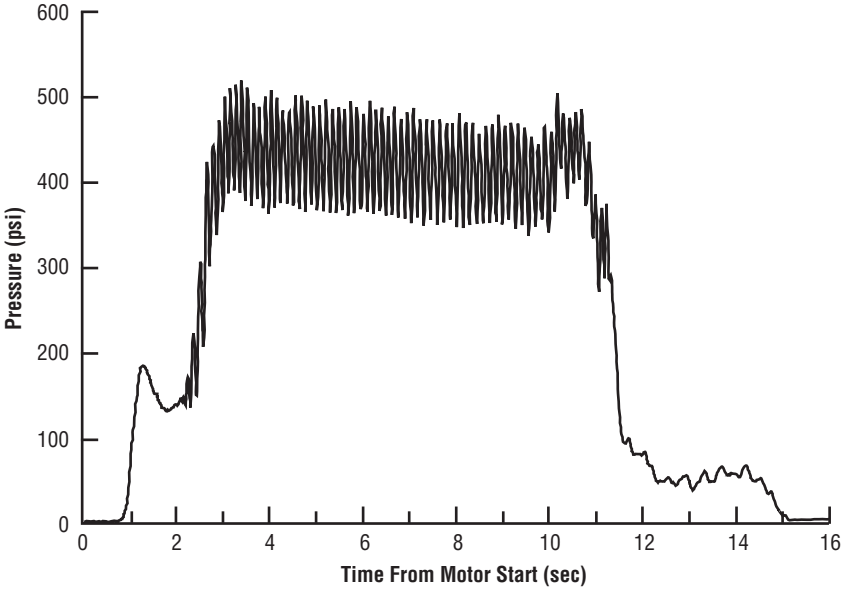

Figure 7. Test 3 chamber pressure.

For test 4, the motor was tested with a used solid fuel grain, a new vaporization chamber with solid fuel fins, and with the JIRAD injector. The motor was accidentally tested with two venturis, in parallel (not shown in figure 4), flowing lox. The resulting lox flow rate was 40 lbm/sec with an injector pressure drop

of 29 percent of chamber pressure. Figure 8 presents chamber pressure for test 4. A chamber pressure of 850 psi was initially achieved. Chamber pressure decreased linearly to 600 psi by the end of the test. Test 4 was stable with small-amplitude, 5-Hz oscillations in chamber pressure.

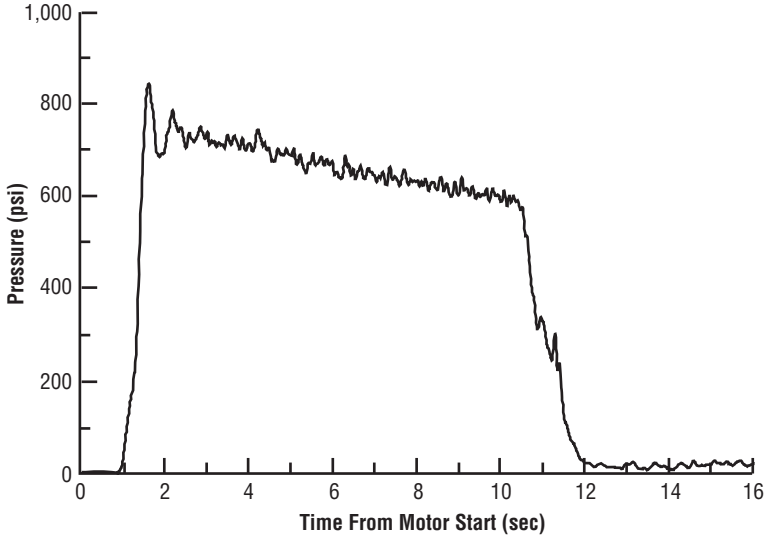

Figure 8. Test 4 chamber pressure.

Test 5 was essentially a repeat of test 3. For this test, the motor was tested with a new solid fuel grain, solid fuel fins in the vaporization chamber, and the JIRAD injector. The lox flow rate was 20 lbm/sec with an injector pressure drop of 13 percent of chamber pressure. Figure 9 presents chamber pressure for test 5. A chamber pressure of 450 psi was achieved. Test 5 was unstable with large-amplitude, 6.5-Hz oscillations in chamber pressure that were sustained throughout the test. The amplitude of the oscillations was ≈25 percent (peak to peak) of chamber pressure.

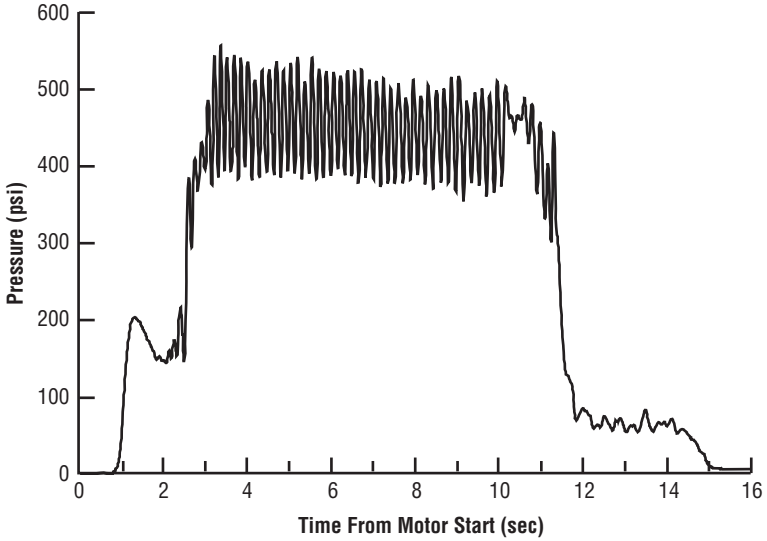

Figure 9. Test 5 chamber pressure.

Test 6 was a repeat of test 4. In test 6, the motor was tested with a used solid fuel grain, a new vaporization chamber with solid fuel fins, and a JIRAD injector. For the test, both valves, which enabled the selection of two different venturis (not shown in fig. 4), were simultaneously opened. The resulting lox flow rate was 40 lbm/sec with an injector pressure drop of 29 percent of chamber pressure. Figure 10 presents chamber pressure for test 6. A chamber pressure of 850 psi was initially achieved. Chamber pressure decreased linearly to 600 psi by the end of the test. Test 6 had marginally stable oscillations in chamber pressure. The amplitude of these oscillations were ≈10 percent (peak to peak) of chamber pressure.

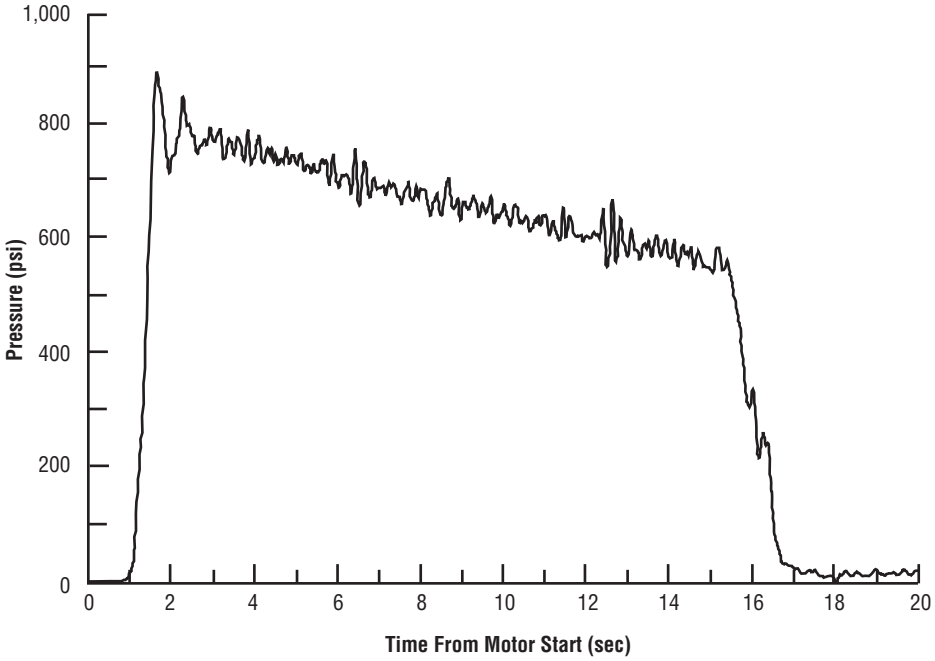

Figure 10. Test 6 chamber pressure.

Test 7 was the second repeat of test 3. For this test, the motor was tested with a new solid fuel grain, solid fuel fins in the used vaporization chamber, and the JIRAD injector. Also, this test was performed with an orifice immediately upstream of the injector. This orifice was intended to decouple the injector and motor from the hydrodynamics of the feedsystem. The lox flow rate was 20 lbm/sec with an injector pressure drop of ≈10 percent of chamber pressure. Figure 11 presents chamber pressure for test 7. A chamber pressure of 450 psi was achieved. Test 7 was stable with small-amplitude oscillations in chamber pressure that were sustained throughout the test. The amplitude of the oscillations was ≈6 percent (peak to peak) of chamber pressure.

The conclusion of the test series was that 24-in. hybrid motors were producing large-amplitude, 6.5-Hz oscillations in chamber pressure that were too low in frequency to be acoustic in nature. Further study of test data indicated that coupling between the combustion chamber and feedsystem hydrodynamics was occurring. This theory was verified in test 7 by decoupling the chamber from the feedsystem with an orifice immediately upstream of the injector. This decoupling resulted in a reduction in the amplitude of chamber pressure oscillations to an acceptable level. Similar results were obtained in subsequent tests by replacing the orifice with an additional cavitating venturi immediately upstream of the injector.

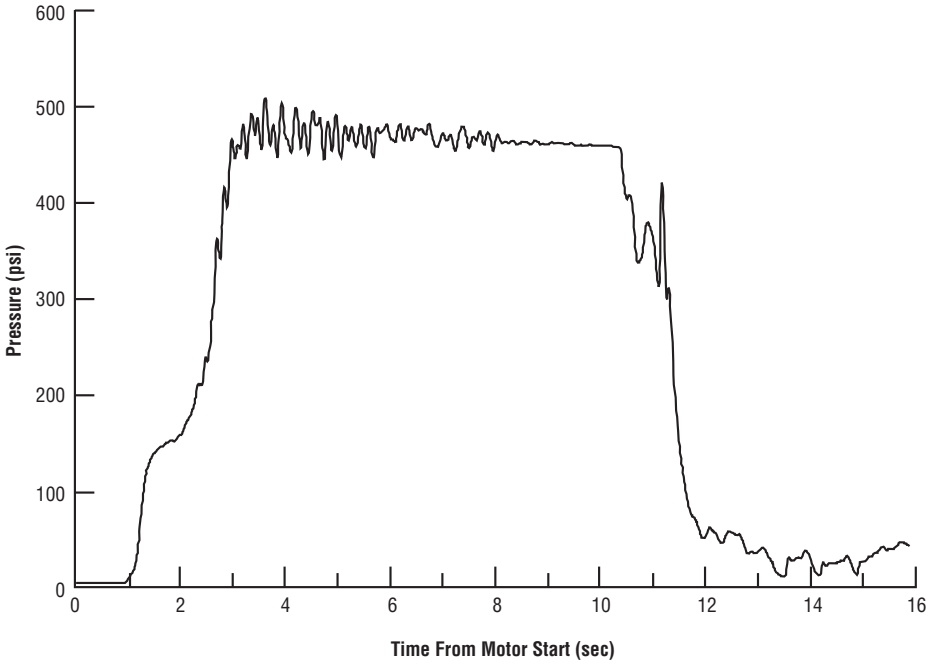

Figure 11. Test 7 chamber pressure.

4. MODELING APPROACH

4.1 Initial Modeling Effort

To investigate nonacoustic combustion instabilities that were exhibited during the test series, joint Thiokol-Rocketdyne collaborators Boardman, Hawkins, Wassom, and Claflin formulated a nonlinear transient model[3,4] of the lox feedsystem and hybrid motor.

The approach consisted of modeling the lox feedsystem and hybrid motor combustion chamber coupled through the lox injector. Features that were modeled in the lox feedsystem were lox compressibility, feedline volume, gaseous oxygen (gox) volume, and unsteady mass conservation. The lox injector was modeled by Bernoulli's equation. Features that were modeled in the hybrid motor combustion chamber were port volume, fuel regression, gas properties, unsteady mass conservation, unsteady energy conservation, gas equation of state, and distributed vaporization.

The transient model was implemented with Matrix-x system simulation software. Matrix-x facilitates on-screen graphical construction of a model of any dynamic system that can be represented by a system of nonlinear ordinary differential equations. A model of a dynamic system is constructed by assembling block elements that represent integrators, gains, adders, multipliers, limiters, etc. Entire subsystems may be assembled in this fashion to form a model of a complex dynamic system.

The model was verified by simulating a 24-in. hybrid motor test performed independently by Thiokol. This test exhibited nonacoustic combustion instabilities similar to those observed in tests 2, 3, and 5 at MSFC. Figure 12 presents a chamber pressure comparison between a simulation generated by the model and test data. Figure 13 presents both the chamber pressure and lox injection pressure simulated by the model. In the model, a "soft" lox feedsystem was assumed. A "soft" feedsystem contains highly compressible lox. The simulation had very good agreement with the test data.

Figure 14 presents both the chamber pressure and lox injection pressure, simulated by the model for a "stiff" feedsystem. A "stiff" feedsystem contains lox that is not as compressible as lox in a "soft" feedsystem. Clearly, lox compressibility in the feedsystem seems to be a factor in determining nonacoustic combustion stability of a hybrid motor.

Funding was exhausted before simulation of the test series, planned to be conducted at MSFC, could be performed.

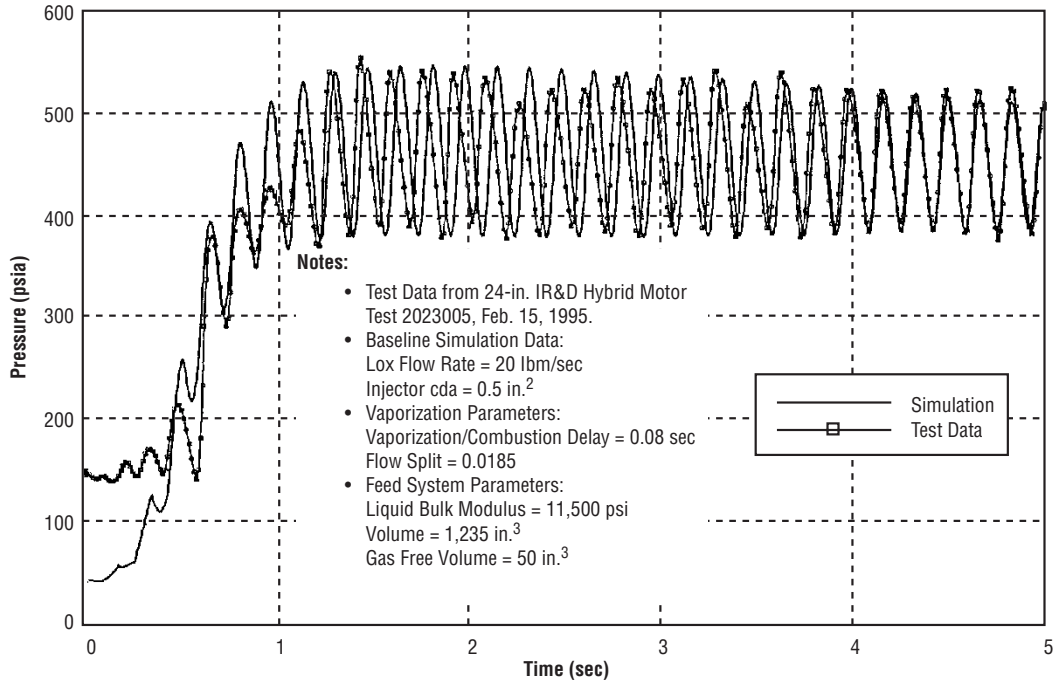

Figure 12. Chamber pressure comparison of a "soft" feedsystem simulation versus test data of a Thiokol independent research and development (IR&D) hybrid motor.

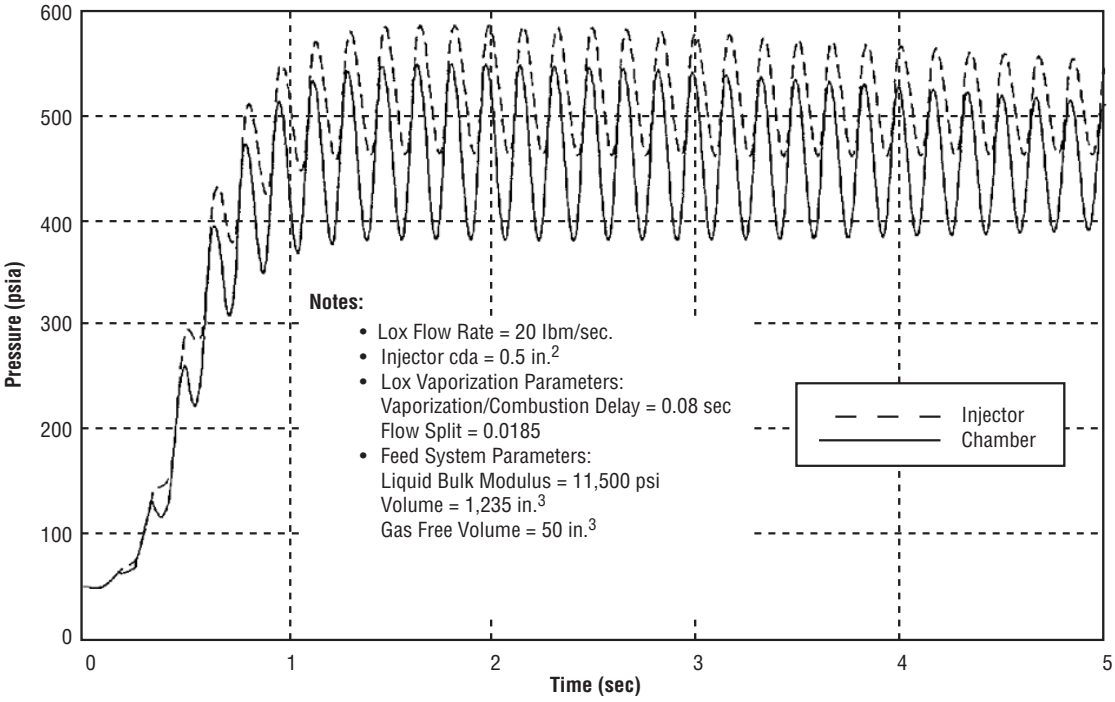

Figure 13. Chamber pressure and lox injection pressure of a "soft" feedsystem simulation of a Thiokol IR&D hybrid motor.

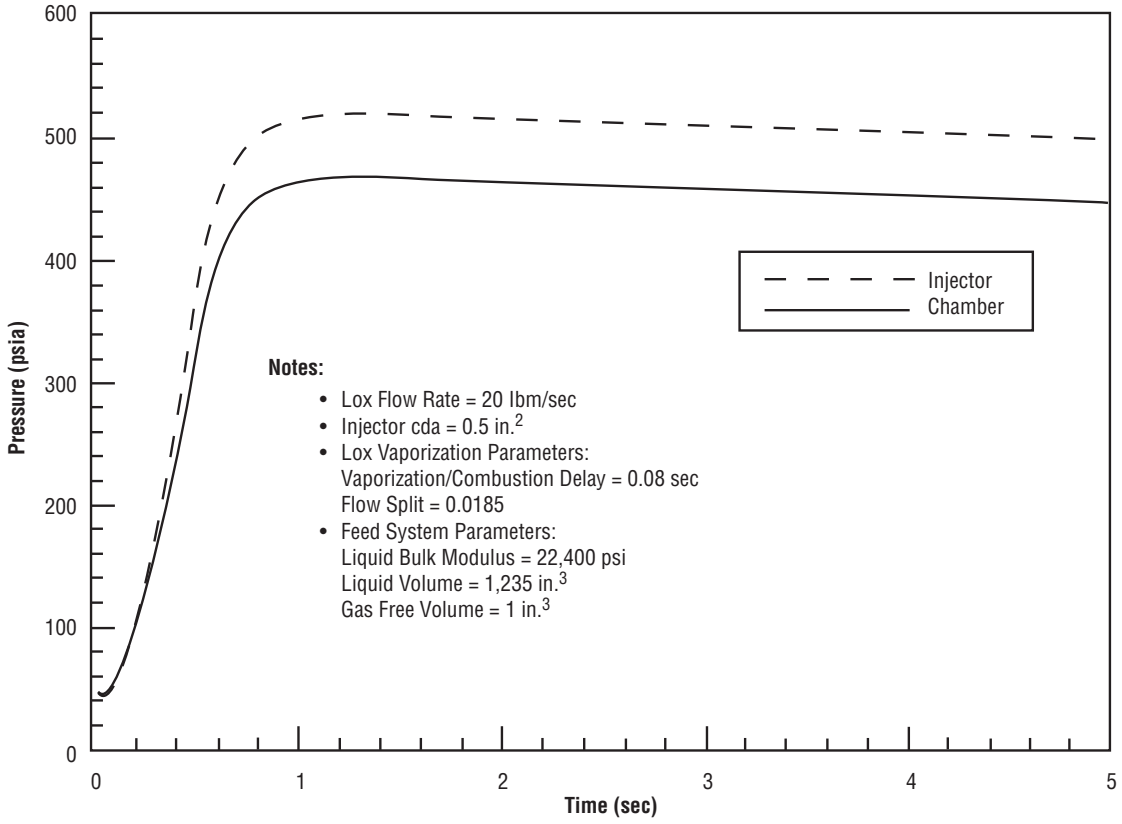

Figure 14. Chamber pressure and lox injection pressure of a "stiff" feedsystem simulation of a Thiokol IR&D hybrid motor.

4.2 Current Modeling Effort

MSFC developed an independent model to investigate nonacoustic combustion instabilities observed in tests 2, 3, and 5. The current model was based on a lumped parameter representation of conservation of mass and energy in the combustion chamber and conservation of mass and momentum in the injector, feedsystem components, and tank. Also, two out of four hybrid combustion instability mechanisms were represented in the current model. The first instability mechanism was atomization/vaporization which was modeled by a time lag. The second instability mechanism was the pressure sensitivity of the regression rate which was modeled by a semiempirical, semitheoretical model. The third instability mechanism, chuffing, was not explicitly modeled. The fourth instability mechanism was vortex shedding which was not represented in the current model. The following paragraphs present details of model formulation.

4.2.1 Combustion Chamber Model

The combustion chamber consisted of the forward vaporization chamber, ports in the solid fuel grain, and aft mixing chamber. Variables and constants in the combustion chamber model were:

A_i total inlet flow area to combustion chamber
A_o lox injector orifice cross-sectional area
A_T nozzle throat cross-sectional area
C_{Pi} gas specific heat at constant pressure
H combustion chamber total enthalpy
H_i total enthalpy of gas entering combustion chamber
ℓ solid fuel port length
$\dot{m}$ nozzle gas flow rate
$\dot{m}_F$ vaporized fuel flow rate
$\dot{m}_i$ flow rate of gas entering combustion chamber
$\dot{m}_o$ gox flow rate
N number of lox injector orifices
n number of solid fuel ports
P_A atmospheric pressure
P_c combustion chamber pressure
r solid fuel port radius
R_i gas constant of gas entering the combustion chamber
T_i temperature of gas entering combustion chamber
V_{AFT} aft mixing chamber volume
V_c combustion chamber volume
V_{FWD} forward vaporization chamber volume
γ gas specific heat ratio
ρ_c combustion chamber gas density
ρ_{SF} solid fuel density.

The combustion model determined pressure and temperature of combustion products in the combustion chamber as functions of time. The behavior of combustion products in the combustion chamber were governed by conservation of mass and energy.

Equation (1) represented conservation of mass:

$$V_c \frac{d\rho_c}{dt} = \dot{m}_o + \left(1 - \frac{\rho_c}{\rho_{SF}}\right) n\dot{m}_F - \dot{m} \quad . \tag{1}$$

The first quantity on the right side of the equation was gox flow rate. Gox flow rate was obtained from the lox injector model and the model of time delay between lox injection and combustion. The second quantity on the right side of the equation was the difference of fuel flow rate due to regression and time rate of mass change in the combustion chamber due to volume increase caused by regression. The third quantity on the right side of the equation was the flow rate of combustion products exiting the combustion chamber through the nozzle.

Equation (2) represented conservation of energy:

$$\frac{V_c}{(\gamma-1)}\frac{dP_c}{dt} = \dot{m}_i H_i - \frac{1}{(\gamma-1)}\frac{P_c}{\rho_{SF}} n\dot{m}_F - \dot{m}H \quad . \tag{2}$$

The first quantity on the right side of the equation was the flow rate of gox total enthalpy. The second quantity on the right side of the equation was the difference of fuel total enthalpy flow rate due to regression and time rate of total energy change in the combustion chamber due to volume increase caused by regression. The third quantity on the right side of the equation was the total enthalpy flow rate of combustion products exiting the combustion chamber through the nozzle.

For both conservation of mass and energy, the nozzle exit flow rate was a function of nozzle pressure ratio as presented in eq. (3):

$$\dot{m} = \rho_c \sqrt{\frac{\gamma P_c}{\rho_c}} A_T \sqrt{\left(\frac{2}{\gamma-1}\right)\left(\frac{P_A}{P_c}\right)^{\frac{2}{\gamma}}\left\{1-\left(\frac{P_A}{P_c}\right)^{\frac{\gamma-1}{\gamma}}\right\}} \quad . \tag{3}$$

The range of pressure ratio was presented in eq. (4):

$$\frac{P_A}{P_c} = \begin{cases} 1 & : \text{ no nozzle flow} \\ \left(\frac{2}{\gamma+1}\right)^{\frac{\gamma}{\gamma-1}} & : \text{ choked nozzle flow} \end{cases} . \tag{4}$$

For the initial and final conditions, the pressure ratio was one, indicating that both the chamber pressure and back pressure were at atmospheric pressure. For the mainstage condition, the pressure ratio was at its critical value, indicating choked flow.

For conservation of energy, total enthalpy of hot gas exiting the nozzle was given in eq. (5):

$$H = \left(\frac{\gamma}{\gamma-1}\right)\frac{P_c}{\rho_c} \quad . \tag{5}$$

Total enthalpy of propellants entering the combustion chamber was given in eq. (6):

$$H_i = C_{Pi}T_i + \frac{1}{2}\left(\frac{R_i T_i}{P_c}\right)^2\left(\frac{\dot{m}_i}{A_i}\right)^2 \quad . \tag{6}$$

Inlet flow rate and inlet flow area were given in eqs. (7) and (8), respectively:

$$\dot{m}_i = \dot{m}_o + n\dot{m}_F \tag{7}$$

and

$$A_i = NA_o + n\left(2\pi r\ell\right). \tag{8}$$

For conservation of mass and energy, the time rate of chamber volume change was proportional to the product of the regression rate and port radius, when eq. (9) was differentiated with respect to time:

$$V_c = V_{\mathrm{FWD}} + V_{\mathrm{AFT}} + n\pi r^2 \ell \quad . \tag{9}$$

Parameters of the combustion chamber model were obtained from the hybrid motor design and operating conditions. The vaporization chamber was cylindrical with a domed head end. Dimensions of the vaporization chamber were 16.8 in. in internal diameter and 20.5 in. in length. The solid fuel grain had seven ports, each with an initial hydraulic diameter of ≈3 in. and a length of 108 in. The aft mixing chamber was cylindrical and was 18.6 in. in internal diameter and 27.4 in. in length. The nozzle was ≈5.7 in. from the inlet to the throat, had a contraction ratio of ≈12.8, and a throat diameter of 2.55 in. for test 1 and 3.60 in. for tests 2 and 3.

Combustion products of lox/HTPB-based fuel combustion, at a mixture ratio of ≈2.3 were assumed to have had a specific heat ratio of 1.137 and a gas constant of 65.2 ft-lb/lbm/°R.

4.2.2 Solid Fuel Ballistics Model

Variables and constants for the solid fuel ballistics model were:

G	gox flux
G_{HIGH}	high gox flux
G_{LOW}	low gox flux
ℓ	fuel port length
m	exponent for pressure
$\dot{m}_F$	fuel flow rate
n	empirical exponent for gox flux
P	chamber pressure
P_{MIN}	atmospheric pressure
r	fuel port radius
$\dot{r}$	regression rate
$\dot{r}_{\mathrm{HIGH}}$	high-pressure regression rate
$\dot{r}_{\mathrm{LOW}}$	low-pressure regression rate
$\dot{r}_{\mathrm{MAX}}$	low-pressure regression rate; maximum value
$\dot{r}_{\mathrm{MIN}}$	high-pressure regression rate; minimum value
ρ_F	solid fuel density.

The solid fuel ballistics model determined both the regression rate and port radius as functions of time. The port fuel flow rate was determined from the product of the port regression rate and port radius as presented in eq. (10):

$$\dot{m}_F = 2\pi\rho_F \ell r\dot{r} \quad . \tag{10}$$

The port regression rate was modeled as a function of port gox flux and chamber pressure.[5] The gox flux dependency of the regression rate was divided into three regimes:

- The first regime corresponded to low gox flux, where radiation heat transfer governed regression rate behavior.

- The second regime corresponded to medium gox flux, where convective heat transfer governed regression rate behavior.

- The third regime corresponded to high gox flux, where combustion chemical kinetics governed regression rate behavior.

In the first and third regimes, the regression rate was sensitive to chamber pressure. In the second regime, the regression rate was dependent on port gox flux alone. The regression rate behavior in the second regime formed the asymptote for high-pressure behavior in the third regime and low-pressure behavior in the first regime. This asymptote for the pressure extremes was

$$\dot{r}(G) = \dot{r}_{\mathrm{MAX}}\left(\frac{G}{G_{\mathrm{LOW}}}\right)^n, \tag{11}$$

and was obtained from the best curve fit of the 24-in. hybrid motor tests conducted under the Hybrid Propulsion Development Program[5] (HPDP), the coefficients were:

G_{LOW} = (2.00 lbm/sec/in.^{2})
n = (0.851621)
$\dot{r}_{\mathrm{MAX}}$ = (0.170 in./sec).

This curve fit for the regression rate closely matched the fifth model out of a collection of nine models presented in the literature.[6]

For eqs. (12)–(16), the coefficients were:

G_{HIGH}= (0.02 lbm/sec/in.^{2})
G_{LOW} = (2 lbm/sec/in.^{2})
m = (0.25)
n = (0.851621)
P_{MIN} = (14.7 psi)
$\dot{r}_{\mathrm{MAX}}$ = (0.170 in./sec)
$\dot{r}_{\mathrm{MIN}}$ = 0.004 in./sec.

The regression rate, as a function of port gox flux and chamber pressure, was defined in the solid ballistics model by:

$$\dot{r}(G,P) = \dot{r}_{\mathrm{LOW}}(G) + \left\{1 - \left(\frac{P_{\mathrm{MIN}}}{P}\right)^{m}\right\}\left\{\dot{r}_{\mathrm{HIGH}}(G) - \dot{r}_{\mathrm{LOW}}(G)\right\} \quad . \tag{12}$$

At low chamber pressures or

$$P \approx P_{\mathrm{MIN}} \quad , \tag{13}$$

the regression rate was given by

$$\dot{r}_{\mathrm{LOW}}(G) = \frac{\dot{r}_{\mathrm{MAX}}}{\left(1 + \frac{G_{\mathrm{LOW}}}{G}\right)^{n}} \quad . \tag{14}$$

At high chamber pressures or

$$P \to \infty \quad , \tag{15}$$

the regression rate was given by

$$\dot{r}_{\mathrm{HIGH}}(G) = \dot{r}_{\mathrm{MIN}}\left(1 + \frac{G}{G_{\mathrm{HIGH}}}\right)^{n} \quad . \tag{16}$$

Figure 15 presents the regression rate as a function of gox flux and chamber pressure, as modeled by eqs. (11), (12), (14), and (16). In the low gox flux regime, the low-pressure limit was the curve fit of 24-in. HPDP test data. The high-pressure limit was constant at 0.0034 in./sec. In the medium gox flux regime, there was no pressure dependency in the regression rate. Therefore, in this regime, the regression rate was based on the curve fit of 24-in. HPDP test data. In the high gox flux regime, the low-pressure limit was 0.17 in./sec. The high-pressure limit was the curve fit of 24-in. HPDP test data.

The above coefficients were selected such that the range of gox flux dependency could be arbitrarily defined about the operating point. The low gox flux regime was defined from zero to ≈0.03 lbm/sec/in.^{2} The medium gox flux regime was defined from ≈0.03 lbm/sec/in.^{2} to ≈1.5 lbm/sec/in.^{2} The high gox flux regime was defined from ≈1.5 lbm/sec/in.^{2} to infinity. Test 1 operating point gox flux was ≈0.2 lbm/sec/in.^{2} Gox flux for test 2 and 3 operating points was ≈0.4 lbm/sec/in.^{2} Both operating points were in the pressure insensitive second regime.

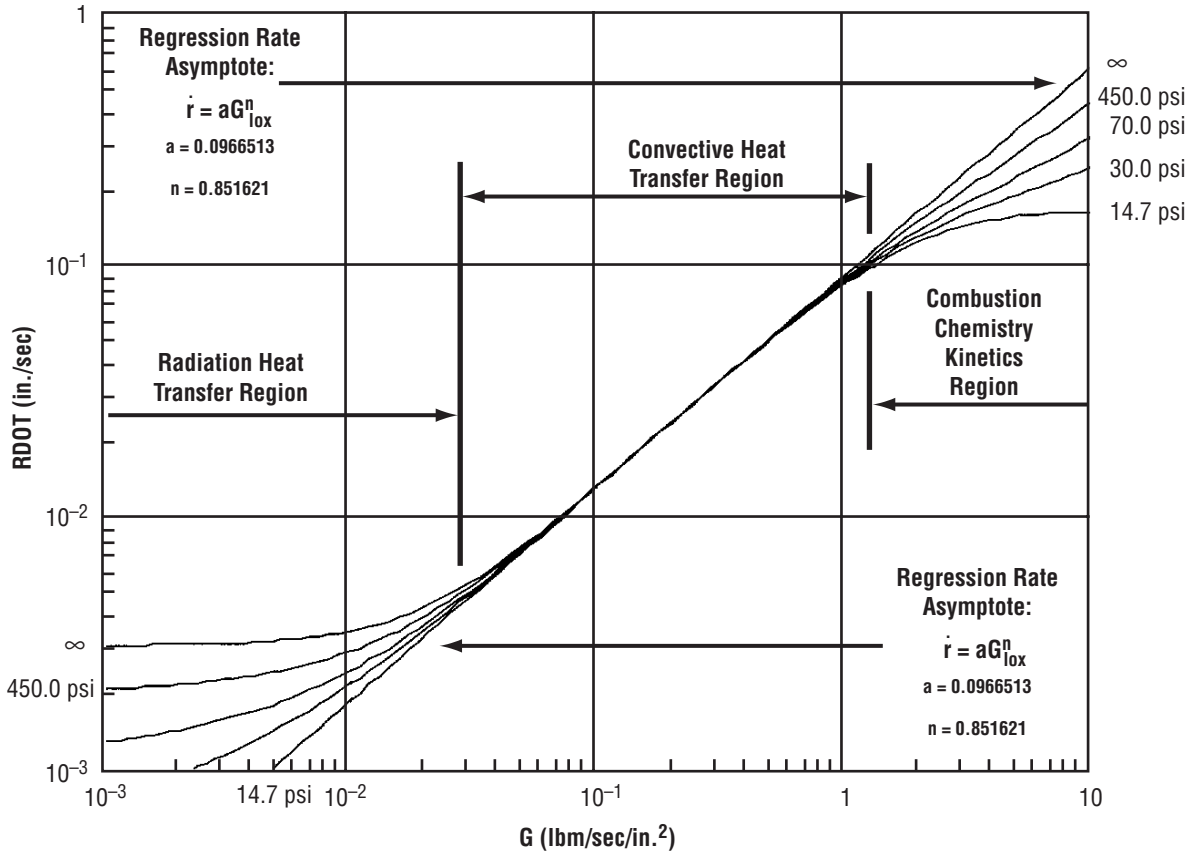

Figure 15. Solid fuel regression model.

According to the regression rate model, test 1 regression rate was ≈0.022 in./sec. However, the actual regression rate for test 1 was ≈0.014 in./sec. Therefore, the regression rates determined by the model were scaled by two-thirds to match the actual regression rate.

Port radius was determined by integrating the port regression rate.

4.2.3 Combustion Stoichiometric Model

Variables and constants for the combustion stoichiometric model were:

f	scaled combustion temperature
P_c	chamber pressure
r	mixture ratio
r_{MAX}	stoichiometric mixture ratio
T_c	combustion temperature
T_{CMAX}	stoichiometric temperature
x	mixture ratio scaled by the stoichiometric value.

The stoichiometric model determined combustion or flame temperature as a function of mixture ratio and chamber pressure. This model was constructed in three steps:

- A series of Thermochemical Equilibrium Program (TEP) calculations for lox/UTF–29901 was performed to determine combustion temperature as a function of mixture ratio for a given chamber pressure. UTF–29901 is an HTPB-based solid motor fuel with composition as shown in table 1.

Table 1. UTF–29901 composition.

Ingredient	Function	Weight Fraction (%)
Escorez 5320 (Polycyclopentadiene)	Fuel	60.00
R–45M (HTPB)	Fuel/binder	30.23
DDI (dimeryl–diisocyanate)	Curative	8.47
C–100 (Isonol)	Crosslinker	0.60
Agerite white–white	Antioxidant	0.50
Carbon black	Opacifier	0.20

The range of mixture ratio considered was from 0.4 to 10. The range of chamber pressure considered was from 14.7 to 1,470 psi.

- From the calculated data, it was observed that all combustion temperature versus mixture ratio curves were scaled by the stoichiometric temperature to a single dimensionless curve. This curve was called the scaled combustion temperature. Also, from the calculated data, it was observed that the stoichiometric temperature that occurred at a mixture ratio of 3.2 varied linearly with the logarithm of the chamber pressure as determined by eq. (17):

$$T_{\mathrm{CMAX}}(P_c) = (617\ ^\circ\mathrm{R})\left(\log\left\{\frac{P_c}{14.7\ \mathrm{psi}}\right\}\right) + (5617\ ^\circ\mathrm{R}) \quad . \tag{17}$$

- The scaled combustion temperature, as a function of mixture ratio, was curve fitted with

$$f(x) = \frac{3x}{2x^{3/2} + 1} \quad , \tag{18}$$

and then combined with the linear curve fit of the stoichiometric temperature to form the combustion temperature model:

$$T_c(P_c, r) = \left\{T_{\mathrm{CMAX}}(P_c) - (530\ ^\circ\mathrm{R})\right\} f\left(\frac{r}{r_{\mathrm{MAX}}}\right) + (530\ ^\circ\mathrm{R}) \quad . \tag{19}$$

For the stoichiometric mixture ratio:

$$r_{MAX} = (3.2) \quad . \tag{20}$$

Figures 16 and 17 compare the combustion temperature model to the thermochemical equilibrium calculation for chamber pressures of 14.7 and 1,470 psi, respectively. Agreement is reasonably good for low mixture ratios and excellent for high mixture ratios. Figure 18 presents combustion temperature, as modeled, as a function of mixture ratio for 14.7, 50, 147, 500, and 1,470 psi.

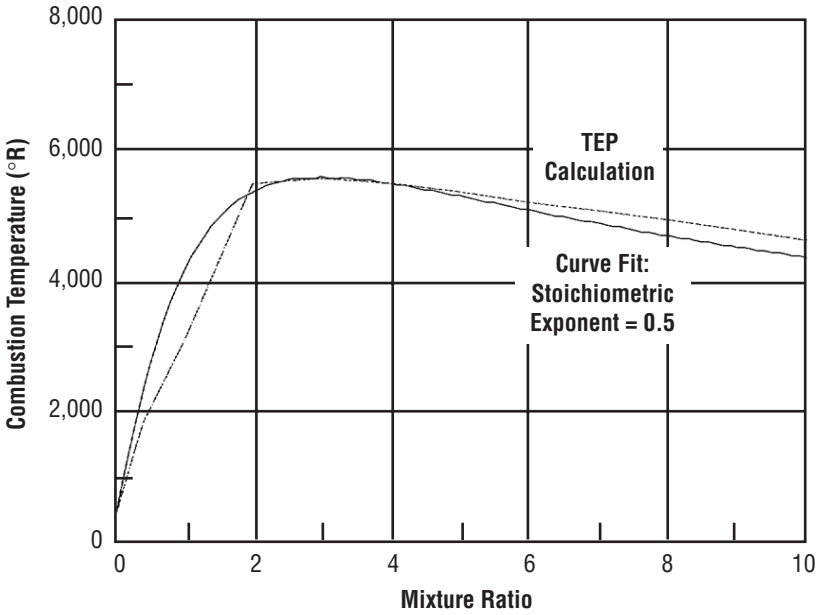

Figure 16. Combustion temperature model for a chamber pressure of 14.7 psi.

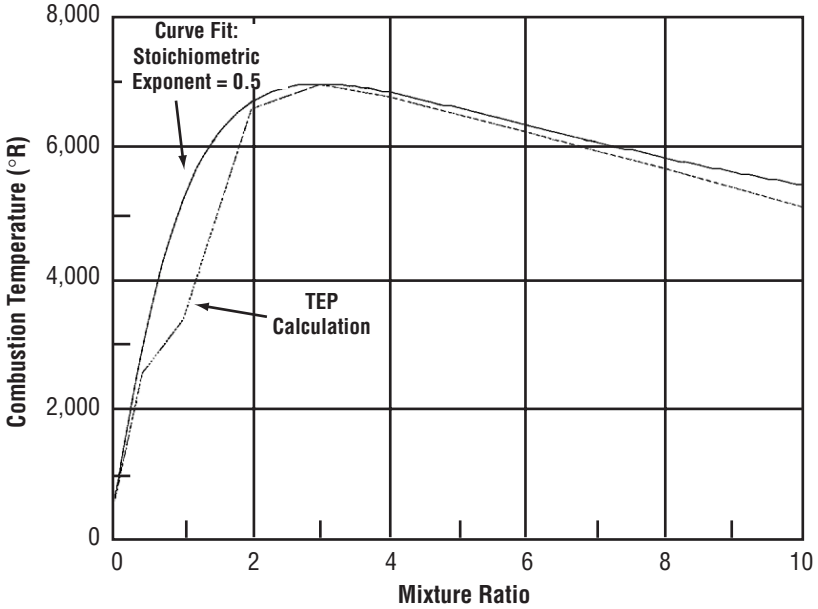

Figure 17. Combustion temperature model for a chamber pressure of 1,470 psi.

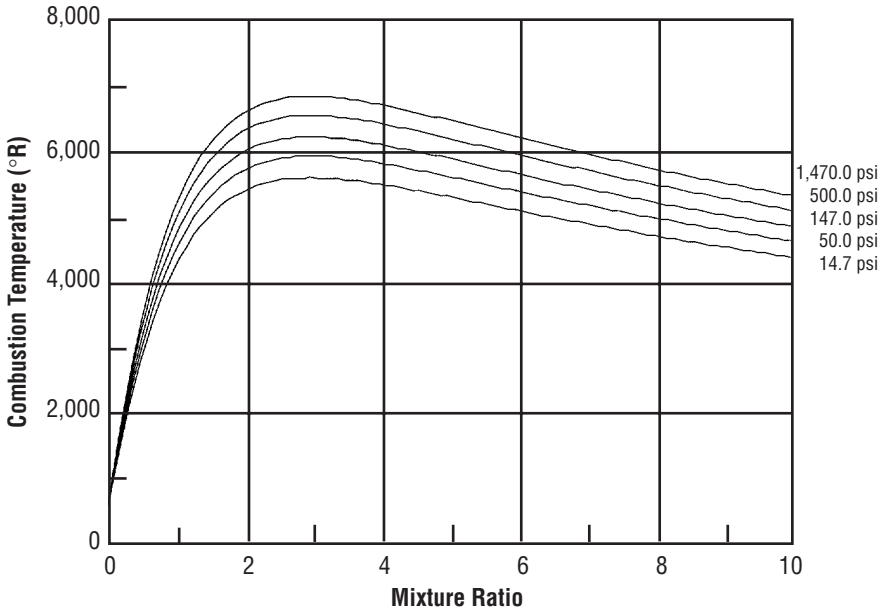

Figure 18. Combustion temperature model for chamber pressures between 4.7 and 1,470 psi.

4.2.4 Lox Injector Model

Variables and constants for the lox injector model were:

A	lox injector orifice cross-sectional area
D	lox injector orifice diameter
f	friction factor
ℓ	lox injector orifice length
$\dot{m}$	lox flow rate through injector orifice
$\dot{m}_o$	lox flow rate into lox dome
N	number of lox injector orifices
P_c	chamber pressure
P_o	lox dome pressure
R_e	orifice Reynolds number
V_o	lox dome volume
ε	orifice surface roughness
μ	lox viscosity
ρ_e	lox injector orifice discharge density
ρ_o	lox dome density.

The behavior of lox in the injector was governed by conservation of mass in the manifold and conservation of linear momentum in each of the orifices.

For the conservation of mass equation, eq. (21):

$$V_o \frac{d\rho_o}{dt} = \dot{m}_o - N\dot{m} \quad , \tag{21}$$

the first quantity on the right side was the lox flow rate entering the manifold. The second quantity on the right side was the total lox flow rate exiting the manifold through injection orifices. On the left side of the equation, the lox density was modeled as a function of pressure at a constant temperature. Therefore, the dependent variable in the mass equation became lox manifold pressure instead of density. Also, a secondary dependent variable was the orifice lox flow rate.

For the conservation of momentum equation, eq. (22):

$$\frac{\ell}{A}\frac{d\dot{m}}{dt} - \left(\frac{1}{\rho_o} - \frac{1}{\rho_e}\right)\left(\frac{\dot{m}}{A}\right)^2 = P_o - P_c - f\frac{\ell}{D}\left(\frac{1}{\rho_o + \rho_e}\right)\left(\frac{\dot{m}}{A}\right)^2 \quad , \tag{22}$$

the first quantity on the right side was the difference in pressure force acting on lox flow in the orifice. The second quantity on the right side was the viscous force acting on the lox flow. The viscous force was described in terms of flow rate and density, therefore, pressure. Since Fanno line flow was assumed in the orifices, friction factor was multiplied by an equivalency factor to account for pressure losses everywhere else in the injector.

The second quantity on the left side of the equation was the difference in lox flow momentum convected through the orifice. If the lox flow rate exiting the orifice was assumed to be the same as the lox flow rate entering the element, then the dependent variable in the momentum equation became lox flow rate. A secondary dependent variable in the momentum equation was lox manifold pressure.

Therefore, the lox injector model consisted of the two equations with the lox manifold or injection pressure and lox injector flow rate as the two unknowns. Additionally, lox injector inlet flow rate and chamber pressure served as the forcing functions.

The lox density was modeled as a linear function of pressure between 14.7 and 3,000 psi at a temperature of 200 °R. This model assumed that lox was slightly compressible. Lox viscosity was also modeled as a linear function of pressure.

Once lox injection flow was determined, a time lag was incorporated to account for conversion of lox to gox. This time lag was the finite amount of time required for most lox droplets to vaporize as they were transported through the vaporization chamber and down through the solid fuel ports.

Figure 19 illustrates the lox injector in the vaporization chamber of the hybrid motor. Parameters of the lox injector model were obtained from designs of the LSSRCS and JIRAD injectors presented in the following paragraphs.

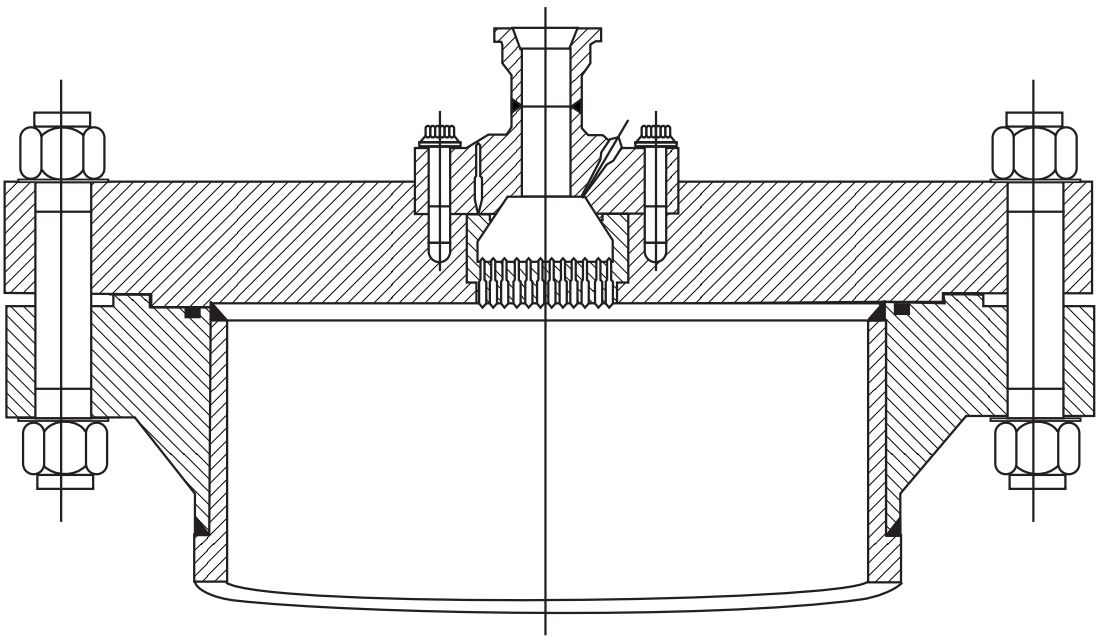

Figure 19. Lox injector in the forward vaporization chamber.

4.2.4.1 LSSRCS Lox Injector Design. Figures 20–23 present the LSSRCS lox injector design. The LSSRCS lox injector was a simple impingement injector with 634 orifices. These orifices were 0.022 in. in diameter in a faceplate that was 0.125 in. thick and 4.745 in. in diameter. The orifices are arranged into 317 doublets, each with a 60° impingement angle. The total lox dome volume, including the volume of the downcomers, was 24 in.^{3}

Figure 20. LSSRCS lox injector.

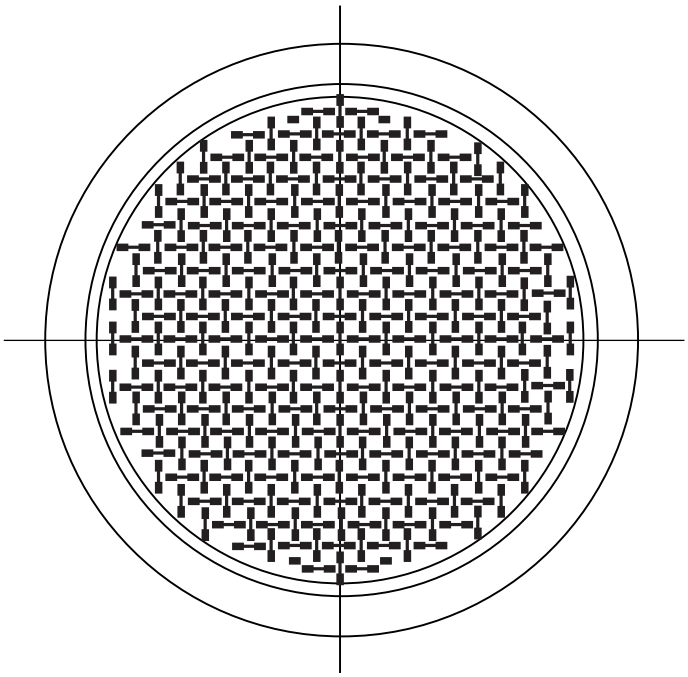

Figure 21. LSSRCS lox injector faceplate design.

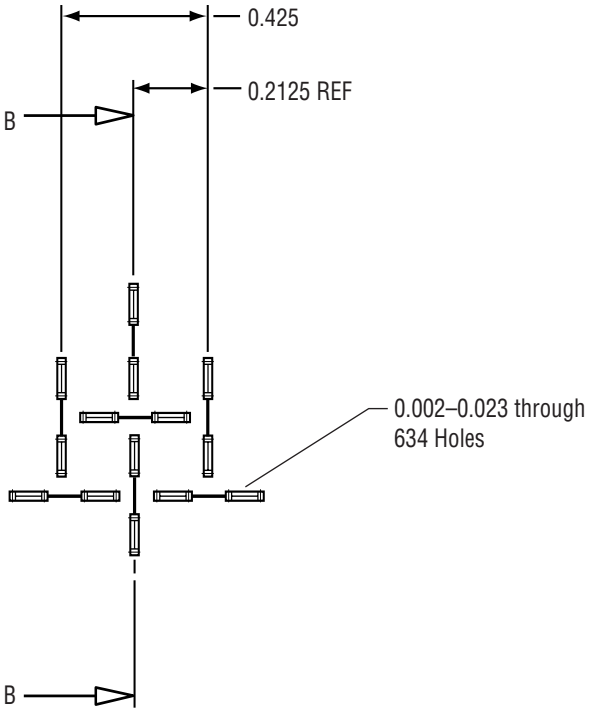

Figure 22. Closeup of the LSSRCS lox injector faceplate impingement pattern (front view).

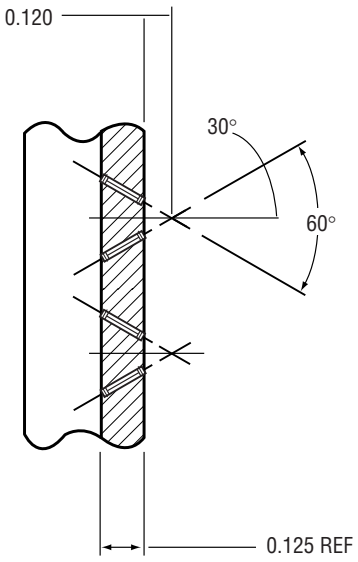

Figure 23. Closeup of the LSSRCS lox injector faceplate impingement pattern (side view).

4.2.4.2 JIRAD Lox Injector Design. Figures 24 and 25 present the JIRAD lox injector and its faceplate design. The JIRAD lox injector was a complex impingement injector with 332 orifices. The orifices were divided into 157 elements of six different element types, A–F.

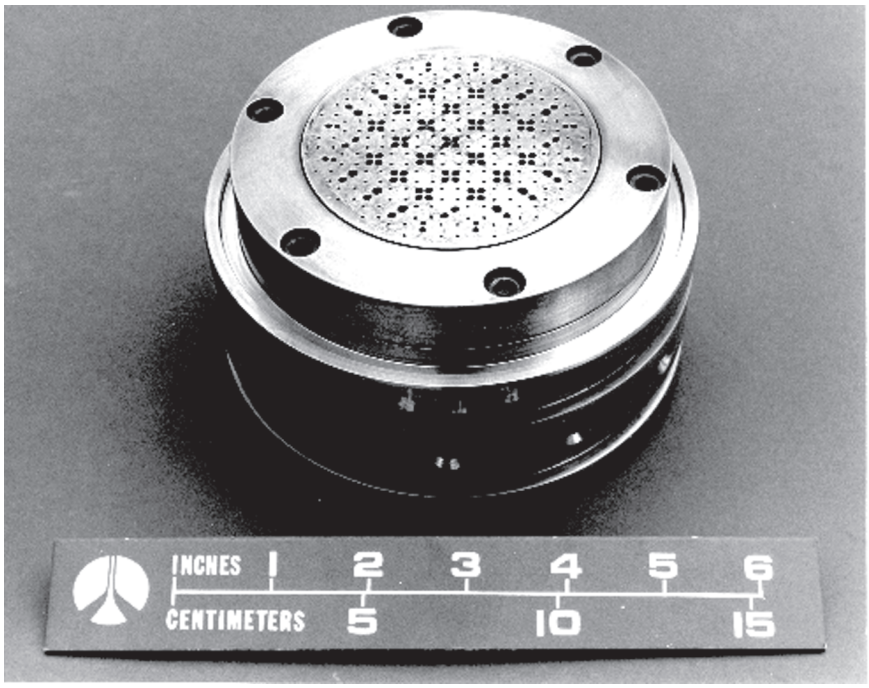

Figure 24. JIRAD lox injector.

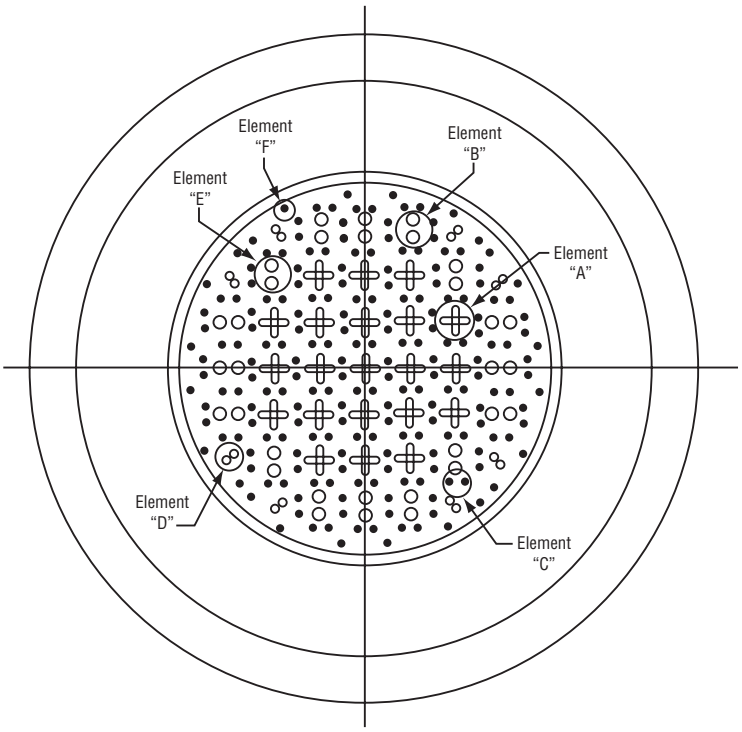

Figure 25. JIRAD lox injector faceplate design.

As presented in figure 26, type A was a quadlet with an orifice diameter of 0.080 in. and a doublet impingement angle of 60°. There were 21 type A elements that provided the primary portion of the core lox flow. As presented in figure 27, type B was a doublet with orifice diameters of 0.100 in. and 0.080 in. with a 60° impingement angle. There were 12 type B elements that provided the secondary portion of the core lox flow.

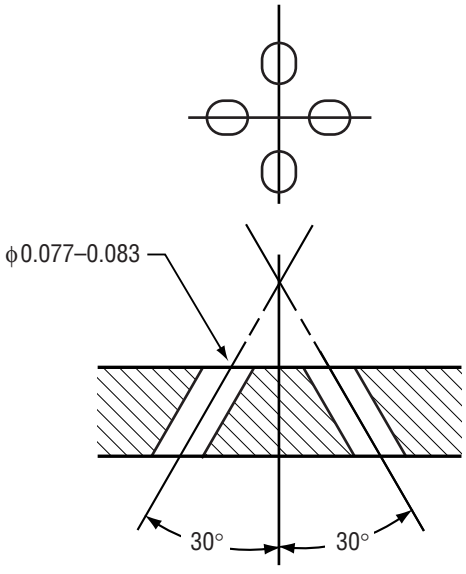

Figure 26. JIRAD injector element type A.

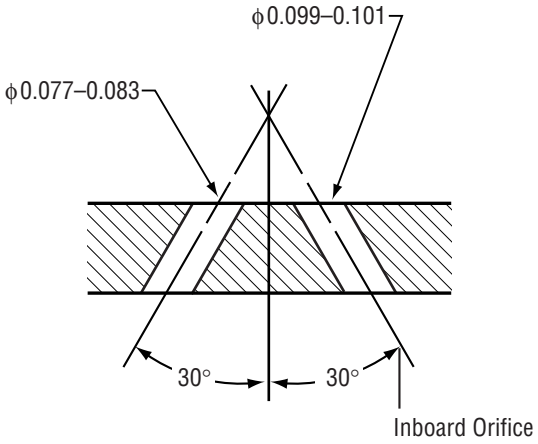

Figure 27. JIRAD injector element type B.

As presented in figure 28, type C was a doublet with an orifice diameter of 0.033 in. and a 60° impingement angle. There were 88 type C elements that surrounded all type A, B, D, and E elements. As presented in figure 29, type D was an atypical doublet with an orifice diameter of 0.064 in. and a 36° impingement angle. One of the two type D orifices was directed axially, the other was angled. There were eight type D elements near the periphery of the injector face.

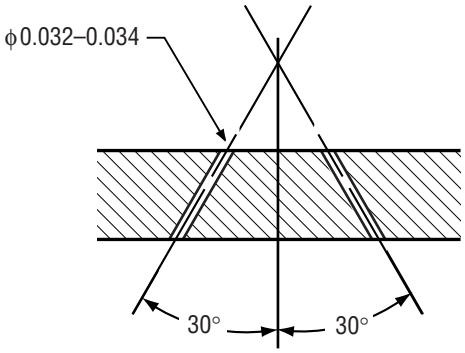

Figure 28. JIRAD injector element type C.

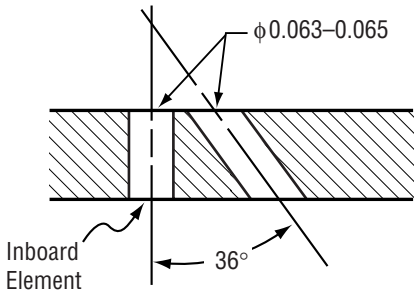

Figure 29. JIRAD injector element type D.

As presented in figure 30, type E was a doublet with an orifice diameter of 0.080 in. and a 60° impingement angle. There were four type E elements located at each of the four corners of the pattern of type A elements. Type D and E elements made up the remainder of the lox core flow. As presented in figure 31, type F was a single orificed element with a diameter of 0.033 in. and angled 30° outboard. There were 24 type F elements at the extreme periphery of the injector face.

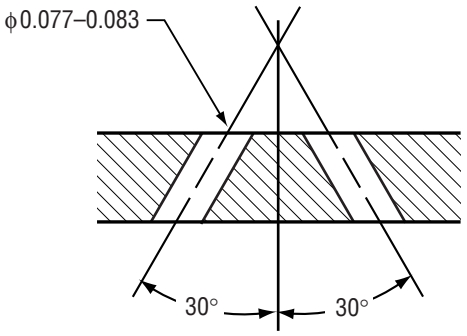

Figure 30. JIRAD injector element type E.

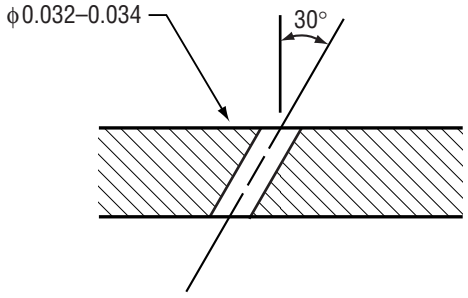

Figure 31. JIRAD injector element type F.

Due to dissimilar orifice diameters, an average hydraulic diameter for the 332 orifices was determined to be ≈0.064 in. Total lox dome volume, including volume of the downcomers, was 17 in.^{3}

4.2.5 Modeling of Vaporization/Combustion Time Lags

To determine time lags for LSSRCS and JIRAD injectors, a vaporization length of 128.5 in. was assumed. This was the combined length of the vaporization chamber and any one of seven ports that a lox droplet traveled before being completely vaporized. From test 1 conditions and from the LSSRCS injector design, an injection velocity of ≈81 ft/sec was determined; therefore, the resulting time lag for test 1 was 0.13 sec. From test 2 conditions and from the JIRAD injector design, an injection velocity of ≈45 ft/sec was determined; therefore, the resulting time lag for test 2 was 0.24 sec.

4.2.6 Modeling of Proportions of Lox Vaporized in the Combustion Chamber

About 16 percent of lox flow was assumed to vaporize instantly in the vaporization chamber. The remaining 84 percent of lox flow was assumed to vaporize later in the ports. These percentages were based on the initial portions of solid fuel surface area in the ports and in the vaporization chamber.

4.2.7 Lox Injector Inlet Model

Variables and constants for the lox injector inlet model were:

A_{AVG}	lox injector inlet fixture; midpoint cross-sectional area
A_e	lox injector inlet fixture; exit cross-sectional area
A_i	lox injector inlet fixture; inlet cross-sectional area
K_{LOSS}	lox injector inlet loss coefficient
ℓ	lox injector inlet fixture length
$\dot{m}$	lox flow rate through injector inlet fixture
$\dot{m}_u$	upstream lox flow rate
P_e	lox injector inlet fixture; exit pressure (lox injection pressure)
P_i	lox injector inlet fixture; inlet pressure
V_{LINE}	upstream lox line volume
ρ_e	lox injector inlet fixture; exit density (lox injection density)
ρ_i	lox injector inlet fixture; inlet density.

The lox injector inlet was a fitting that mated the lox feedline to the lox injector. This fitting could have been a diffuser that would have mated an oversized feedline to the injector. This fitting could also have been s-shaped to mate the feedline and the injector, which could have been at different elevations. This fitting could have been a combination of the former and the latter. The model of the lox injector inlet accounted for pressure losses due to these possibilities. Equations for conservation of mass and momentum for the lox injector inlet model were:

$$V_{\mathrm{LINE}} \frac{d\rho_i}{dt} = \dot{m}_u - \dot{m} \tag{23}$$

and

$$\frac{\ell}{A_{\mathrm{AVG}}} \frac{d\dot{m}}{dt} - \left(\frac{1}{\rho_i} \frac{A_{\mathrm{AVG}}}{A_i} - \frac{1}{\rho_e} \frac{A_{\mathrm{AVG}}}{A_e} \right) \left(\frac{\dot{m}}{A_{\mathrm{AVG}}} \right)^2 = P_i - P_e - K_{\mathrm{LOSS}} \left(\frac{1}{\rho_i + \rho_e} \right) \left(\frac{\dot{m}}{A_{\mathrm{AVG}}} \right)^2 . \tag{24}$$

Formulation of the lox injector inlet model was similar to the lox injector model with five differences:

- There were multiple, yet identical, injector element flow rates to consider in the lox injector model. There was a single flow rate to consider in the lox injector inlet model.

- Inlet and exit cross-sectional areas of each orifice were identical in the lox injector model. Cross-sectional areas of the inlet and exit may have been different in the lox injector inlet model.

- Fanno line flow was assumed to account for pressure losses in the orifices in the lox injector model. A friction factor multiplier was assumed to account for pressure losses everywhere else in the injector. Fanno line flow was not assumed at all in the lox injector inlet model. An empirical loss coefficient was assumed to account for all pressure losses.

- Volume in the mass equation for the lox injector model corresponded to the lox manifold. Volume in the mass equation for the lox injector inlet model corresponded to the length of feedline that extended upstream from the lox injector inlet to the next feedline component, which would have been the lox valve.

- Pressure-forcing functions in the lox injector model were lox injector manifold pressure and chamber pressure. Pressure-forcing functions in the lox injector inlet model were feedline pressure between the injector inlet and valve and lox injector manifold pressure.

The lox injector inlet consisted of a nozzle that contracted to mate the 3-in. feedline to a 2-in. opening into the injector manifold. This contraction took place over a 5-in. length. A 90° bend was immediately upstream of the nozzle. Although the nozzle and the bend both accounted for losses in pressure, most of the loss occurred in the nozzle. About 32.8 in. of 3-in. feedline were between the injector inlet and the valve upstream.

4.2.8 Lox Valve Model

Variables and constants for the lox valve model were:

A lox valve orifice cross-sectional area (varies with time)
D lox valve orifice diameter (varies with time)
f friction factor
K_{EQUIV} lox valve loss equivalence coefficient
ℓ lox valve orifice length
$\dot{m}$ lox valve flow rate
$\dot{m}_u$ upstream lox flow rate
P_e lox valve exit pressure
P_i lox valve inlet pressure
V_{LINE} upstream lox line volume
ρ_e lox valve exit density
ρ_i lox valve inlet density.

Conservation of mass and momentum equations for the lox valve model were:

$$V_{\text{LINE}} \frac{d\rho_i}{dt} = \dot{m}_u - \dot{m} \tag{25}$$

and

$$\frac{\ell}{A}\frac{d\dot{m}}{dt} - \left(\frac{1}{\rho_i} - \frac{1}{\rho_e}\right)\left(\frac{\dot{m}}{A}\right)^2 = P_i - P_e - K_{\text{EQUIV}} f \frac{\ell}{D}\left(\frac{1}{\rho_i + \rho_e}\right)\left(\frac{\dot{m}}{A}\right)^2 \quad . \tag{26}$$

Formulation of the lox valve model was also similar to the lox injector model with four differences:

- There were multiple, yet identical, flow rates to consider in the lox injector model. Like the lox injector inlet model, there was a single flow rate to consider in the lox valve model.

- The cross-sectional area of each orifice was fixed in the lox injector model. The cross-sectional area of the orifice in the lox valve model varied with time as the valve opened and closed.

- Volume in the mass equation for the lox injector model corresponded to the lox manifold. Volume in the mass equation for the lox valve model corresponded to the length of feedline that extended upstream from the lox valve to the next feedline component, which would have been the lox venturi.

- Pressure forcing functions in the lox injector model were lox injector manifold pressure and chamber pressure. Pressure forcing functions in the lox valve model were feedline pressure between the injector inlet and valve and feedline pressure between the valve and venturi.

A globe valve design was assumed for the lox valve. The globe valve was assumed to have a flow passage with a maximum open diameter of 3 in. and a length of 1 in. Pressure loss across the valve was determined by the loss equivalency coefficient of 340 for globe valves. The lox valve was assumed to take 0.5 sec to fully open and 1 sec to completely close. Between the valve and the venturi upstream, there was 238.8 in. (19.9 ft) of 3-in. feedline.

4.2.9 Lox Venturi Model

Variables and constants for the lox venturi model were:

A_{AVG}	lox venturi midpoint cross-sectional area
A_e	lox venturi exit cross-sectional area
A_i	lox venturi inlet cross-sectional area
D	lox feedline diameter
d	lox venturi throat diameter
k_{LOSS}	lox venturi inlet loss coefficient
K_{LOSS}	lox venturi total loss coefficient
ℓ	lox venturi throat length

$\dot{m}$ lox venturi flow rate
$\dot{m}_{\text{CHK}}$ choked lox venturi flow rate
$\dot{m}_{\text{UNCHK}}$ unchoked lox venturi flow rate
$\dot{m}_u$ upstream lox flow rate
P_e lox venturi exit pressure
P_i lox venturi inlet pressure
P_v lox vapor pressure
V_{LINE} upstream lox line volume
ρ_e lox venturi exit density
ρ_i lox venturi inlet density.

Mass and momentum conservation equations for the lox venturi model were:

$$V_{\text{LINE}} \frac{d\rho_i}{dt} = \dot{m}_u - \dot{m} \quad , \tag{27}$$

$$\dot{m} = \begin{cases} \dot{m}_{\text{UNCHK}} : \dot{m}_{\text{UNCHK}} < \dot{m}_{\text{CHK}} \\ \dot{m}_{\text{CHK}} : \dot{m}_{\text{UNCHK}} \geq \dot{m}_{\text{CHK}} \end{cases} \quad . \tag{28}$$

$$\frac{\ell}{A_{\text{AVG}}} \frac{d\dot{m}_{\text{UNCHK}}}{dt} - \left(\frac{1}{\rho_i} \frac{A_{\text{AVG}}}{A_i} - \frac{1}{\rho_e} \frac{A_{\text{AVG}}}{A_e} \right) \left(\frac{\dot{m}_{\text{UNCHK}}}{A_{\text{AVG}}} \right)^2 = P_i - P_e - K_{\text{LOSS}} \left(\frac{1}{\rho_i + \rho_e} \right) \left(\frac{\dot{m}_{\text{UNCHK}}}{A_{\text{AVG}}} \right)^2 \tag{29}$$

and

$$\dot{m}_{\text{CHK}} = \rho_e \sqrt{\frac{1}{1 + k_{\text{LOSS}} - \left(\frac{d}{D} \right)^4}} \sqrt{\frac{2\left(P_i - P_v \right)}{\rho_e}} A_e \quad . \tag{30}$$

Formulation of the lox venturi model was similar to the lox injector model with four differences:

- There were multiple, yet identical, flow rates to consider in the lox injector model. Like the models of the lox injector inlet and the lox valve, there was a single flow rate to consider in the lox venturi model.

- The momentum equation in the lox injector model was implemented as a differential equation to be solved for lox flow rate as a function of time. The momentum equation was not only implemented as a differential equation in the lox venturi model, but in the form of Bernoulli's equation as well. Bernoulli's equation would determine steady lox flow rate from the difference in pressure upstream of the venturi and vapor pressure of oxygen at the venturi throat. The steady lox flow rate, determined from Bernoulli's equation, would limit the lox flow rate determined from the differential equation; therefore, cavitation in the venturi would be modeled.

- Volume in the mass equation for the lox injector model corresponded to the lox manifold. Volume in the mass equation for the lox venturi model corresponded to the length of feedline that extended upstream from the lox venturi to the lox tank.

- Pressure-forcing functions in the lox injector model were lox injector manifold pressure and chamber pressure. Pressure-forcing functions in the lox venturi model were feedline pressure between the venturi and valve and feedline pressure between the venturi and lox tank.

The venturi for test 1 had a nozzle that contracted from a 3-in. inlet diameter to a 0.259-in. throat diameter. The nozzle angle was 37° and the length from the venturi inlet to the downstream end of the throat was 4.197 in. The test 1 cavitating venturi design assumed an upstream pressure of 1,250 psi to set the lox flow rate at ≈10 lbm/sec.

The venturi for tests 2, 3, and 7 had a nozzle that contracted from a 3-in. inlet diameter to a 0.376-in. throat diameter. The nozzle angle was 37° and the length from the venturi inlet to the downstream end of the throat was 4.372 in. The test 2 cavitating venturi design assumed an upstream pressure of 1,125 psi to set the lox flow rate at ≈20 lbm/sec.

The resulting discharge coefficient for both venturis was 0.93. Both venturis were assumed to cavitate at 85.013 psi at a lox temperature of 200 °R. About 223 ft of 3-in. feedline was between the venturi and the tank upstream.

4.2.10 Lox Tank Flow Model.

Variables and constants for the lox tank flow model were:

A	local lox tank cross-sectional area
A_E	lox tank exit line cross-sectional area
A_T	lox tank cross-sectional area
g	gravitational acceleration
P	local lox pressure within tank
P_E	lox tank exit line pressure
P_T	lox tank ullage pressure
u	local lox velocity within tank
$\dot{Z}$	lox tank liquid level velocity
Z	lox tank liquid level
Z_{MAX}	initial lox tank cross-sectional area
Z_o	vertical position of lox tank bottom
ρ_L	lox density.

Behavior of lox flow from the tank was governed by conservation of mass and momentum for an incompressible fluid where

$$u(z,t) = \frac{A(Z)}{A(z)}\dot{Z} \tag{31}$$

and

$$\frac{\partial u}{\partial t} + u\frac{\partial u}{\partial z} = -\frac{1}{\rho_L}\frac{\partial P}{\partial z} - g \quad . \tag{32}$$

Fluid flow was assumed to be quasi-one dimensional. From conservation of mass, presented in eq. (31), liquid velocity at any vertical position in the tank was determined from tank cross-sectional area at that vertical position, tank cross-sectional area at the liquid surface, and rate of fall of the liquid surface. The lox tank was assumed to be cylindrical in geometry such that

$$A(z) = \begin{cases} A_T : z > Z_0 \\ A_E : z < Z_0 \end{cases} , \tag{33}$$

where, for the tank and its discharge line cross-sectional areas,

$$A_T > A_E \quad . \tag{34}$$

Local liquid velocity was determined from conservation of momentum by solving the partial differential equation. Integrating the momentum equation in the vertical direction, from some reference level below the tank to the liquid level, gave liquid acceleration integrated from the reference level to the liquid surface as proportional to the difference in the total head. The constant of proportionality was gravitational acceleration. The reference level was taken to be the vertical position of the feedline. Substituting for liquid velocity locally at the feedline level and at the liquid surface gave a second-order, nonlinear, ordinary differential equation where the liquid level was the unknown. This second-order ordinary differential equation is presented as a set of two first-order ordinary differential equations:

$$\frac{dx_1}{dt} = x_2 \tag{35}$$

and

$$\frac{dx_2}{dt} = -\frac{\frac{1}{2}\left\{1 - \left(\frac{A_T}{A_E}\right)^2\right\}x_2^2 + gx_1 + \frac{1}{\rho_L}\left(P_T - P_E\right)}{x_1 + \left(\frac{A_T}{A_E} - 1\right)Z_0} , \tag{36}$$

where

$$x_1 = z \ , \tag{37}$$

and

$$x_2 = \dot{Z} \ , \tag{38}$$

Pressure-forcing functions for the lox tank model were ullage pressure and feedline pressure below the tank for the following initial conditions:

$$x_1(0) = Z_{\mathrm{MAX}} \ , \tag{39}$$

$$x_2(0) = 0 \ , \tag{40}$$

and

$$gZ_{\mathrm{MAX}} + \frac{1}{\rho_L}\left\{P_T(0) - P_E(0)\right\} = 0 \ . \tag{41}$$

The liquid surface in the lox tank was assumed to be at rest and at a liquid level that corresponded to a liquid volume that was 97 percent of total tank volume. The liquid was assumed to be initially at hydrostatic equilibrium.

4.2.11 Lox Tank Ullage Model.

Constants and variables for the behavior of gas in the lox tank ullage were:

A_T	lox tank cross-sectional area
H	lox tank height
$\dot{m}_G$	gaseous nitrogen flow rate
P_0	lox tank ullage reference gas pressure
P_G	lox tank ullage gas pressure
T_0	lox tank ullage gas temperature
V_G	lox tank ullage volume
Z	lox tank liquid level
Z_0	lox tank bottom level
$\dot{Z}$	lox tank liquid level velocity
ρ_0	lox tank ullage reference gas density
ρ_G	lox tank ullage gas density.

Ullage pressure was determined from conservation of mass in the lox tank ullage by:

$$\frac{d}{dt}\left(\rho_G V_G\right) = \dot{m}_G \ , \tag{42}$$

$$V_G = A_T(H + Z_0 - Z) \ , \tag{43}$$

$$\rho_G = \frac{P_G}{P_0}\rho_0 \ , \tag{44}$$

and

$$P_G = \rho_G RT_0 \quad . \tag{45}$$

Gaseous nitrogen (GN_2) was discharged into the ullage to maintain ullage pressure as ullage increased in volume. The increase in ullage volume was due to the falling liquid surface as the lox tank discharged. GN_2 in the ullage was assumed to expand isothermally. GN_2 in the ullage and the lox was assumed to be in thermal equilibrium at 200 °R.

Substituting eqs. (43), (44), and (45) into eq. (42) and solving for the time rate of change of the ullage gas pressure gave:

$$\frac{dP_G}{dt} = \frac{RT_0\dot{m}_G + P_G A_T \dot{Z}}{A_T\left(H + Z_0 - Z\right)} \quad . \tag{46}$$

GN_2 flow rate was controlled by a pressure regulator that was modeled as a first-order system. Input to the pressure regulator model was the error between desired ullage pressure and actual ullage pressure. This error was the amount that the lox tank was underpressurized and was limited such that the resulting GN_2 flow rate was always positive. This assumed that the tank was not vented to prevent overpressurization. For every psi that the tank was underpressurized, 2 lbm/sec of GN_2 flow rate was ordered. The time constant of the first-order pressure regulator model was assumed to be 0.1 sec. The time constant represented the agility of the lox tank pressure transducer and pressure regulator servo.

The 3,000-gal lox tank was spherical with an internal diameter of ≈9 ft. The lox tank was elevated 9.3 ft above the lox feedline. To simplify the tank geometry for modeling, a cylindrical tank geometry was assumed. The cylindrical lox tank was ≈8 ft in height and diameter and was elevated 9.3 ft above the lox feedline. The initial conditions for the lox tank liquid level was that it was at rest at ≈17 ft above the feedline. The lox tank was initially pressurized to ≈1,250 psi for test 1 and ≈1,125 psi for tests 2, 3, and 7.

4.2.12 Matrix-x Simulation Software Example

Constants and variables for the Matrix-x simulation of a mass-spring-damper system were:

c	mass-scaled damping constant
f_0	mass-scaled driving force constant
k	mass-scaled spring constant
u	unit step function
x_1	position
x_2	velocity
ε	mass-scaled nonlinear spring constant.

With equations governing the dynamics of the hybrid motor and lox feedsystem established, the Matrix-x simulation software was implemented to perform the time-accurate simulation. Instead of discussing the lengthy details of this implementation, it is more appropriate to demonstrate how the Matrix-x simulation software was used to simulate a simple mass-spring-damper dynamic system.

Figure 32 illustrates the mass-spring-damper system. The mass-spring-damper system was governed by the equation set:

$$\frac{dx_1}{dt} = x_2 \tag{47}$$

and

$$\frac{dx_2}{dt} = -kx_1 - cx_2 + \varepsilon x_1^3 + f_0 u(t) \quad . \tag{48}$$

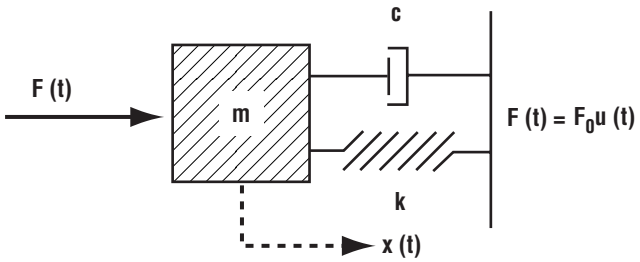

Figure 32. Mass-spring-damper model.

A nonzero value of ε indicated that the spring was nonlinear. Since the mass was at rest and was not displaced, the equation set was subject to the initial conditions:

$$x_1(0) = 0 \tag{49}$$

and

$$x_2(0) = 0 \quad . \tag{50}$$

The mass-scaled coefficients for the case of a linear spring were:

c = (4.39823/sec)
f_0 = (986.96044 ft/sec^2)
k = (986.96044/sec^2)
ε = 0.

Selection of mass-scaled coefficients for the linear spring assumed a natural frequency of 5 Hz and a damping ratio of 0.07.

For the case of the nonlinear spring, the mass-scaled coefficients were identical to those of the linear spring with the exception of a nonzero value of ε and were as follows:

$$
\begin{aligned}
c &= (4.39823/\text{sec}) \\
f_0 &= (986.96044\ \text{ft/sec}^2) \\
k &= (986.96044/\text{sec}^2) \\
\varepsilon &= (21.25/\text{ft}^2\text{sec}^2).
\end{aligned}
$$

Figure 33 presents the Matrix-x graphical representation of the nonlinear mass-spring-damper model. Close examination of figure 33 revealed that it was simply a graphical representation of eqs. (47) and (48), subject to the initial conditions in eqs. (49) and (50). Figure 34 presents simulation results of the linear mass-spring-damper system. Figure 35 presents simulation results of the nonlinear mass-spring-damper system.

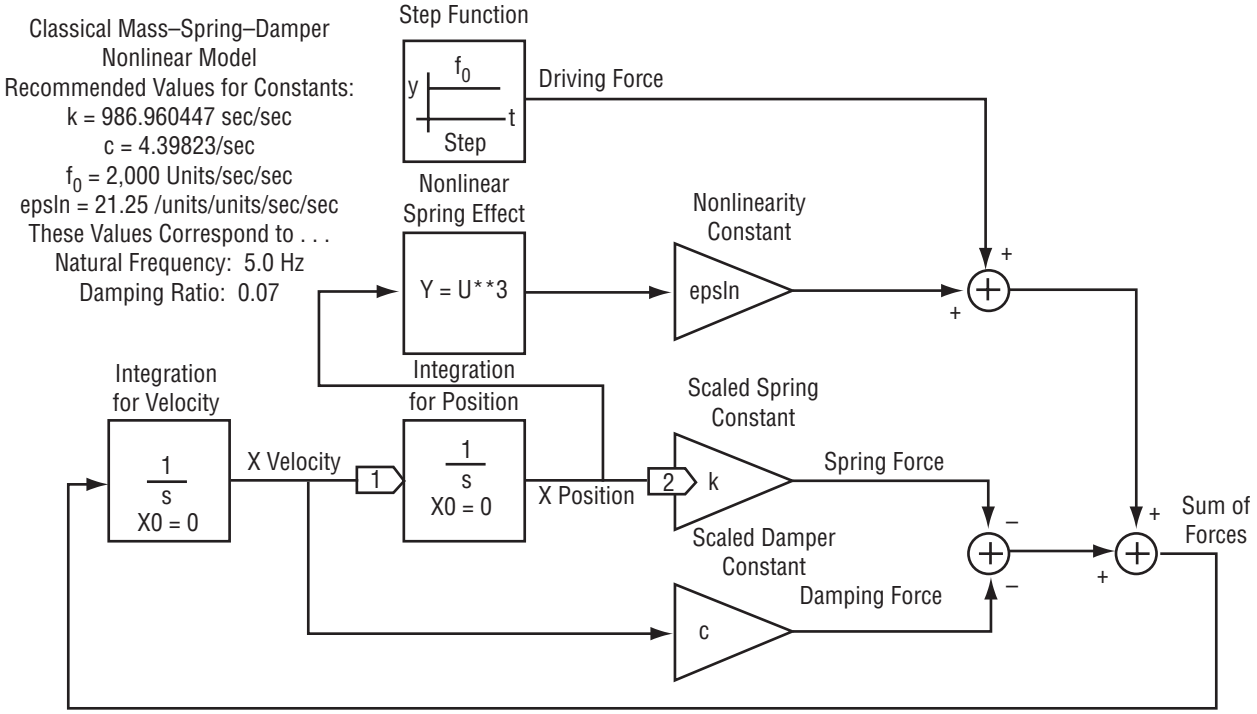

Figure 33. Matrix-x model of the mass-spring-damper system.

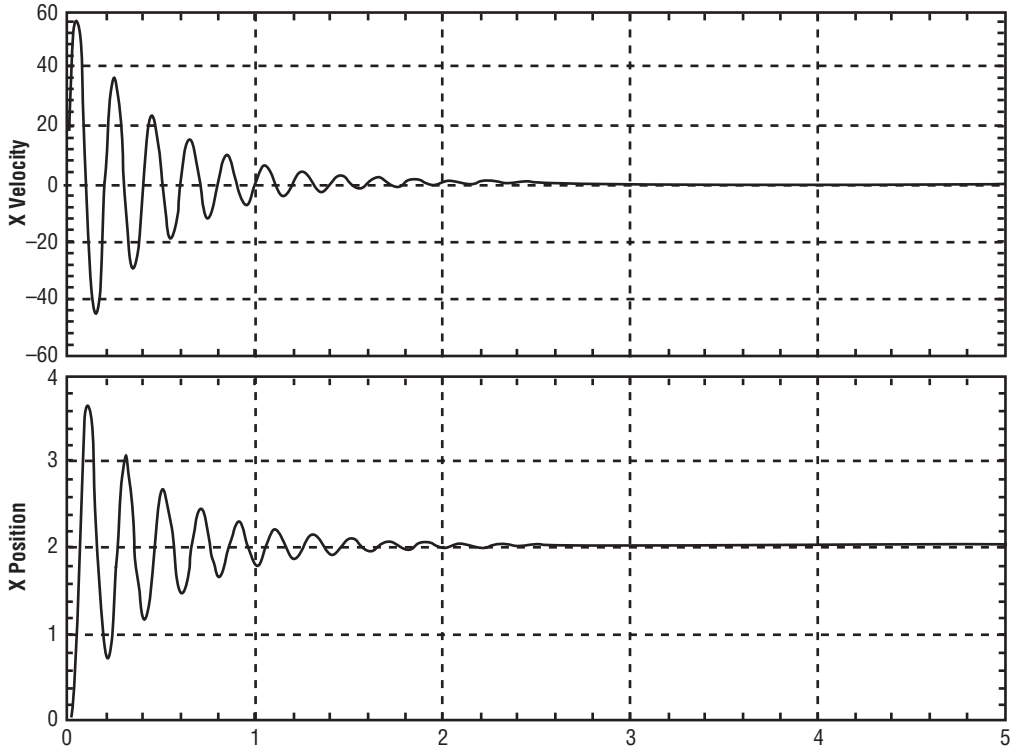

Figure 34. Mass velocity and position for the linear mass-spring-damper simulation.

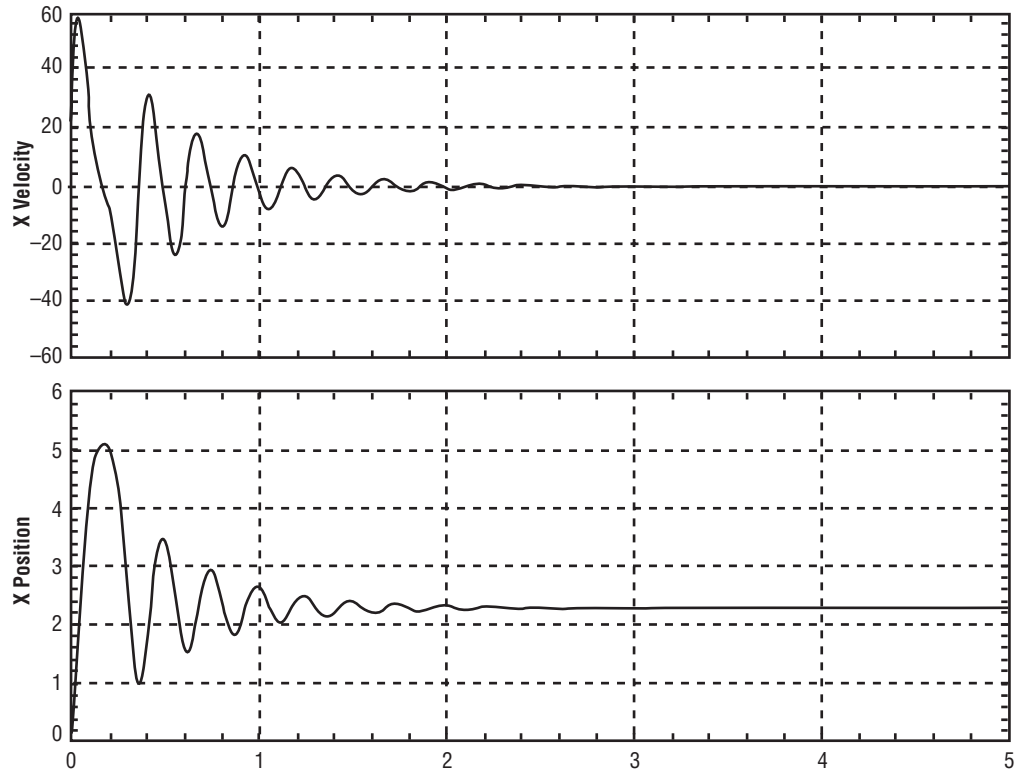

Figure 35. Mass velocity and position for the nonlinear mass-spring-damper simulation.

Differences between the linear and nonlinear cases were determined by examination of figures 34 and 35. For example:

- Where the velocity was exactly sinusoidal in the linear case, the velocity was only approximately sinusoidal in the nonlinear case.

- Peak amplitude in position was less in the linear case than in the nonlinear case.

- Frequency of oscillations was a constant of 5 Hz in the linear case.

- For the nonlinear case, frequency increased in time from an initial value of ≈3 Hz during the first second to ≈4 Hz during the next second.

Hence, the mass-spring-damper model illustrated how Matrix-x was used to simulate a dynamic system described by a set of first-order, nonlinear, ordinary differential equations.

5. RESULTS OF TEST SIMULATIONS

5.1 Results of the Test 2 Simulation

Figures 36 and 37 present actual and simulated test data for test 2. Recall that test 2 was performed with the same fuel grain used in test 1, a lox flow rate of 20 lbm/sec, and the low-impedance JIRAD injector with a pressure drop of 11 percent. Pressures presented in both figures corresponded to the upstream venturi pressure, injection pressure, and chamber pressure. There was a very good qualitative match between actual and simulated test data. Chamber pressure oscillations were initially at 20 percent of mean chamber pressure in amplitude and decayed gradually by the end of the test.

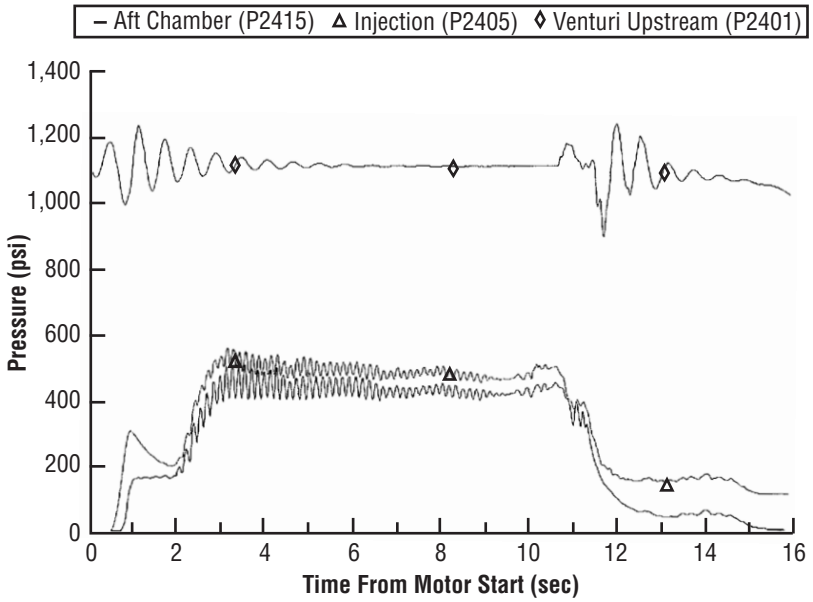

Figure 36. Actual system pressures from test 2.

Chamber pressure oscillations in actual test data were reported to have a frequency of ≈6.5 Hz. Figure 38 presents a frequency spectrum of the simulated chamber pressure. Peaks occurred in the spectrum at 2.5, 6.4, and 10.4 Hz. The peak at 2.5 Hz was primary in spectral intensity and corresponded to the "fill/flush" frequency. The peak at 6.4 Hz was slightly secondary in spectral intensity and corresponded to the nonacoustic combustion instability associated with the lox feedline between the valve and injector. The peak at 10.4 Hz was a distant third in spectral intensity and did not correspond to any known cause.

Test 2 was simulated first since it was the first unstable test. The first few attempts at simulating test 2 resulted in nonoscillatory pressures in the combustion chamber and feedsystem downstream of the venturi. Upstream of the venturi, feedsystem pressure was oscillatory due to the "water hammer" effect. It was also noticed that, according to figure 4, feedline volume upstream of the venturi was enormous. If oscillations in feedsystem pressure were caused by a large feedline volume, then feedline volume downstream of the venturi had to be increased to cause oscillations in feedsystem pressure downstream of the venturi.

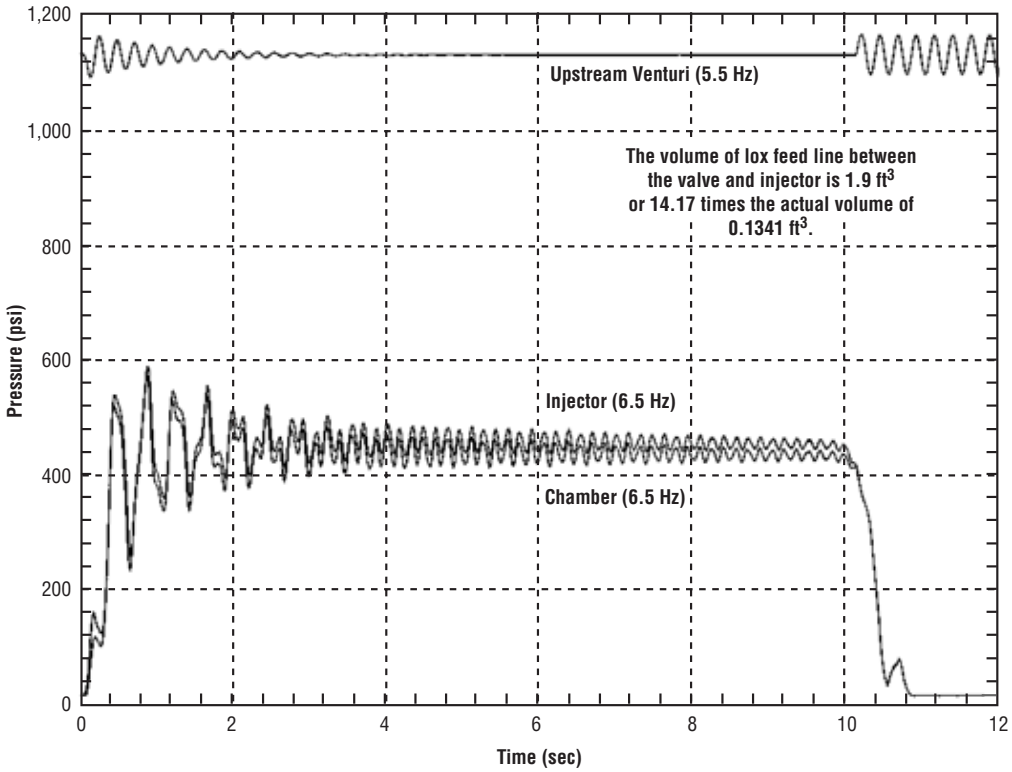

Figure 37. Simulated system pressures for test 2.

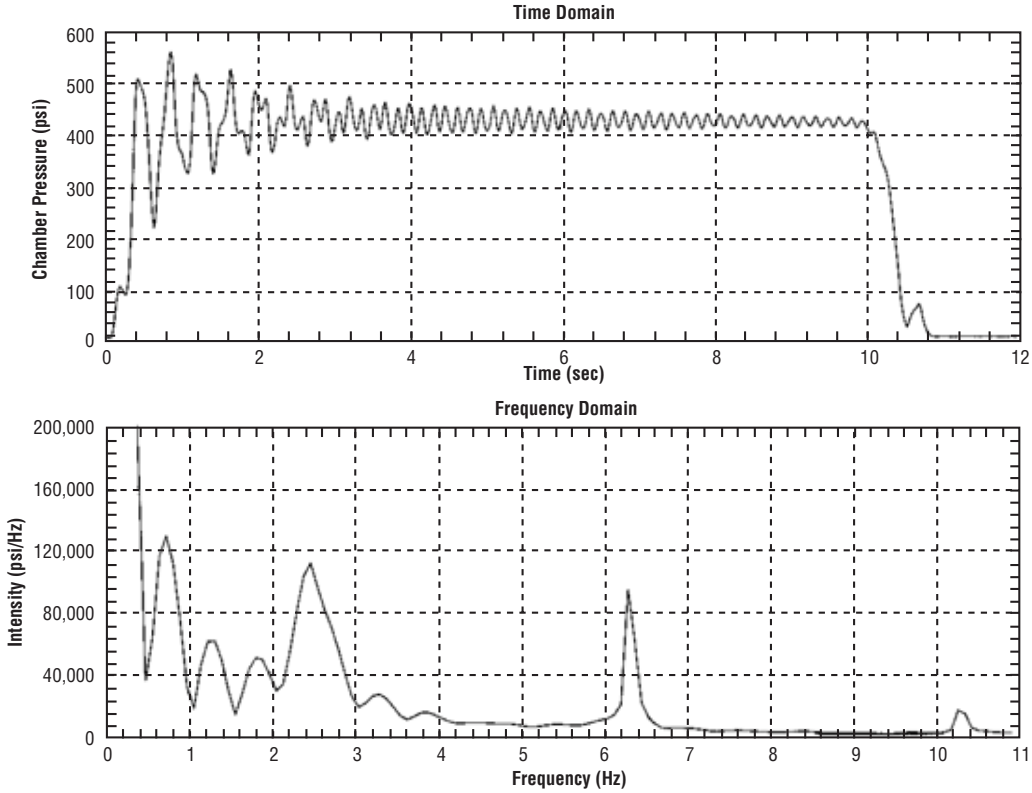

Figure 38. Simulated chamber pressure and frequency spectrum for test 2.

Therefore, feedline volume downstream of the venturi, between the valve and injector, was increased 14.17 times the actual value. This increase was equivalent to the actual lox compressibility being 14.17 times the compressibility as was modeled. The large compressibility in this portion of feedline suggested presence of trapped gox. This increase resulted in pressure oscillations in the chamber and in the feedsystem downstream of the venturi. These oscillations were initially at 20 percent of mean chamber pressure in amplitude and decayed gradually by the end of the test.

Capacitance[7] is the product of feedline volume and compressibility. Increasing volume, compressibility, or both resulted in increased capacitance. Stiffness is the reciprocal of capacitance. It was a small capacitance or a large stiffness that resulted in a "stiff" feedsystem, making oscillations in the feedsystem impossible. It was a large capacitance or a small stiffness that resulted in a "soft" feedsystem, making oscillations in the feedsystem possible.

5.2 Results of the Test 3 Simulation

Figures 39 and 40 present actual and simulated test data for test 3. Recall that test 3 was performed with a fresh fuel grain, a lox flow rate of 20 lbm/sec, and the low-impedance JIRAD injector with a pressure drop of 14 percent. As in test 2, there was a very good qualitative match between actual and simulated test data. Chamber pressure oscillations were initially at 25 percent of mean chamber pressure in amplitude and were sustained throughout the test. Chamber pressure oscillations in actual test data were reported to have a frequency of ≈7.5 Hz.

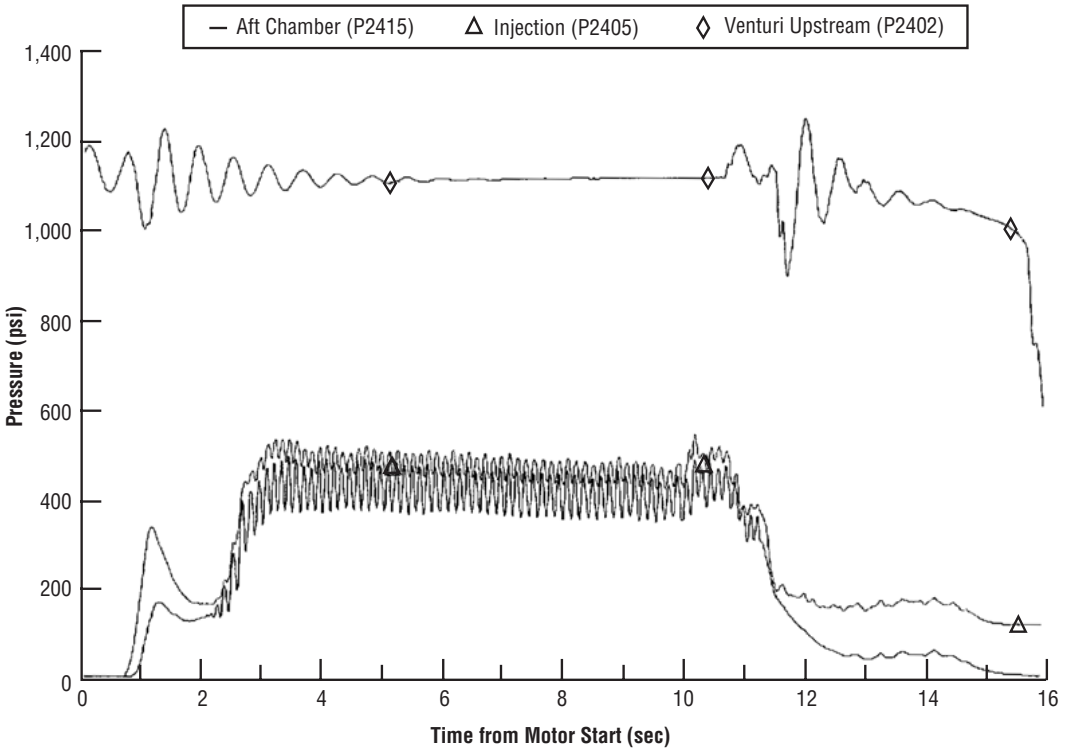

Figure 39. Actual system pressures from test 3.

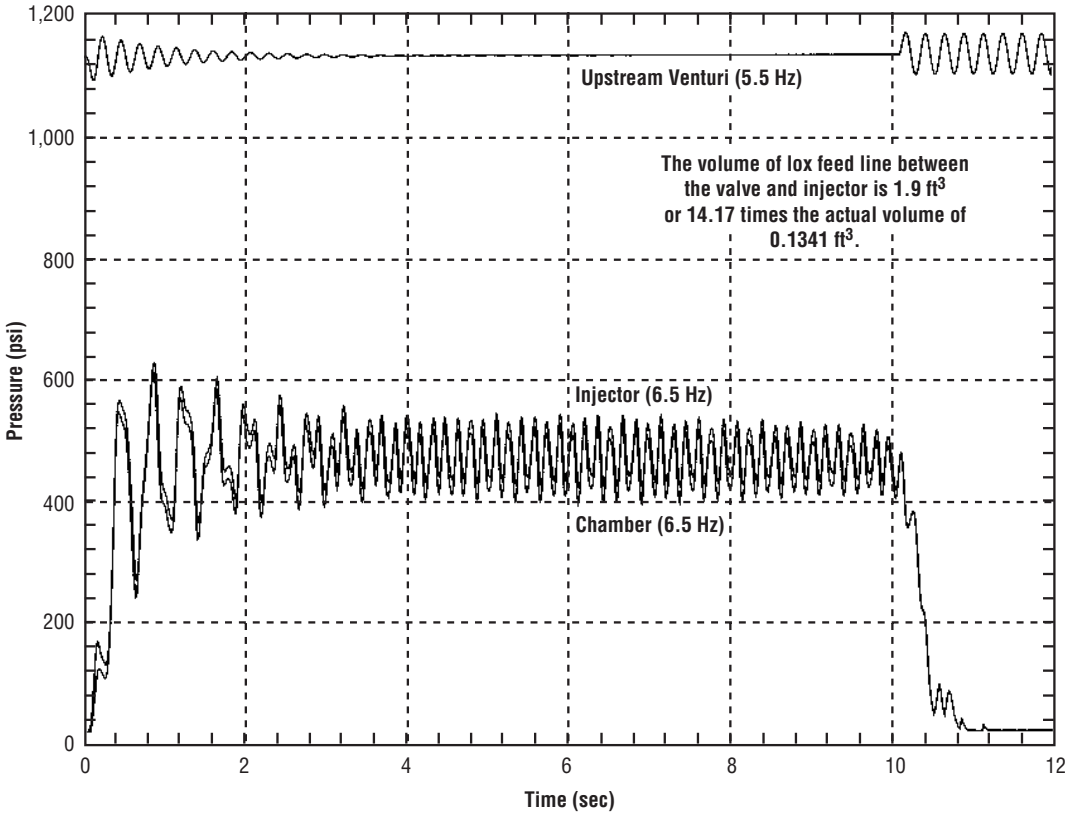

Figure 40. Simulated system pressures for test 3.

Figure 41 presents a frequency spectrum of the simulated chamber pressure. As in figure 38 for test 2, there were peaks in the spectrum at 2.5, 6.4, and 10.4 Hz. The peak at 2.5 Hz was secondary in spectral intensity and corresponded to the "fill/flush" frequency. The peak at 6.4 Hz now dominated in spectral intensity and corresponded to the nonacoustic combustion instability associated with the lox feedline between the valve and injector. Dominance of the peak in spectral intensity at 6.4 Hz seemed to be related to the fact that the oscillations in pressure were sustained in test 3. The peak at 10.4 Hz was a distant third in spectral intensity and still did not correspond to any known cause.

Test 3 was simulated second for two reasons: (1) Test 3 was the second unstable test, and (2) the only difference between tests 2 and 3 was that while test 2 was performed with a used fuel grain, test 3 was performed with a new fuel grain.

The first attempt at simulating test 3 resulted in nonoscillatory pressures in the combustion chamber and feedsystem downstream of the venturi. Like test 2, feedline volume downstream of the venturi between the valve and injector was increased 14.17 times the actual value. This increase was equivalent to actual lox compressibility being 14.17 times the compressibility as was modeled. This increase resulted in pressure oscillations in the chamber and feedsystem downstream of the venturi. These oscillations were initially at 25 percent of mean chamber pressure in amplitude and were sustained throughout the test.

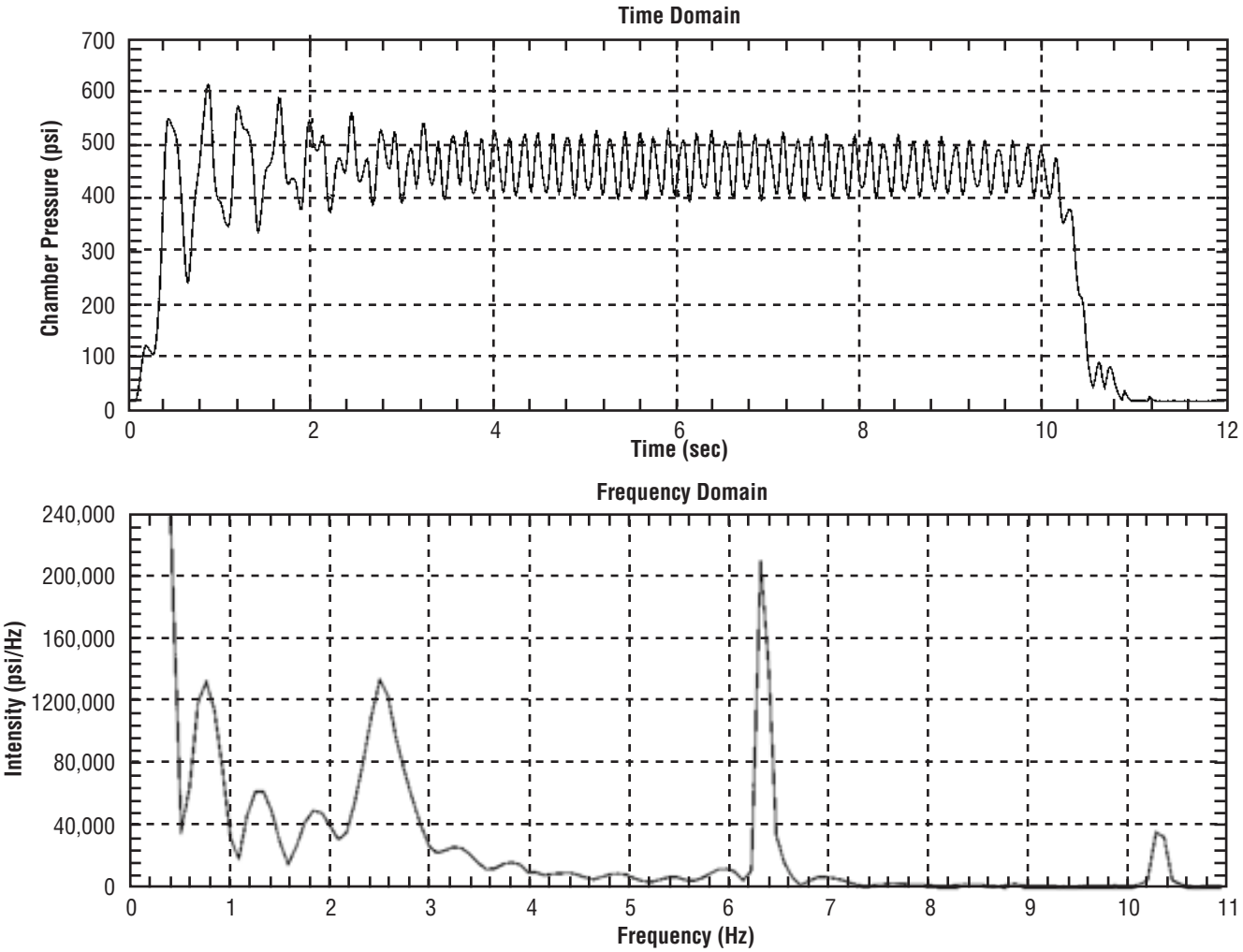

Figure 41. Simulated chamber pressure and frequency spectrum for test 3.

5.3 Results of the Test 1 Simulation

Figures 42 and 43 present actual and simulated test data for test 1. Recall that test 1 was performed with a fresh fuel grain, a lox flow rate of 10 lbm/sec, and the high-impedance LSSRCS injector with a pressure drop of 44 percent. As in tests 2 and 3, there was a very good qualitative match between actual and simulated test data. There were no chamber pressure oscillations throughout the test.

Figure 44 presents a frequency spectrum of the simulated chamber pressure. There were minor peaks and humps in the spectrum at 0.9, 1.6, 2.3, 2.9, 3.4, 4, and 4.7 Hz. Spectral intensity of the peaks and humps seemed to decrease with increasing frequency. These peaks and humps seemed to be associated with the mean transient of chamber pressure. These same peaks and humps in the spectral intensity appeared in some degree in the spectra of tests 2 and 3.

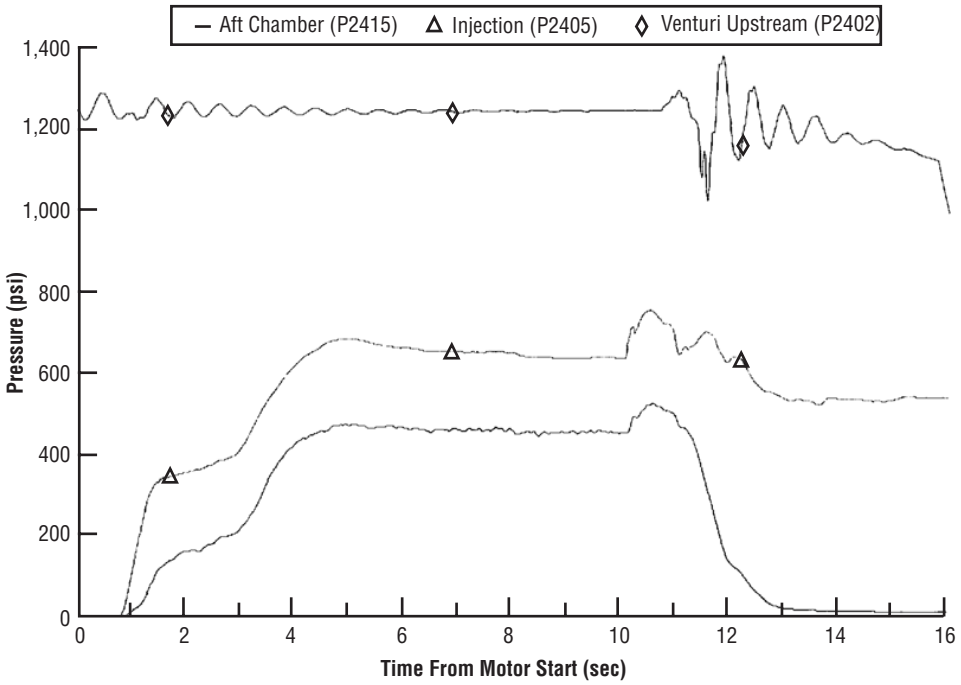

Figure 42. Actual system pressures from test 1.

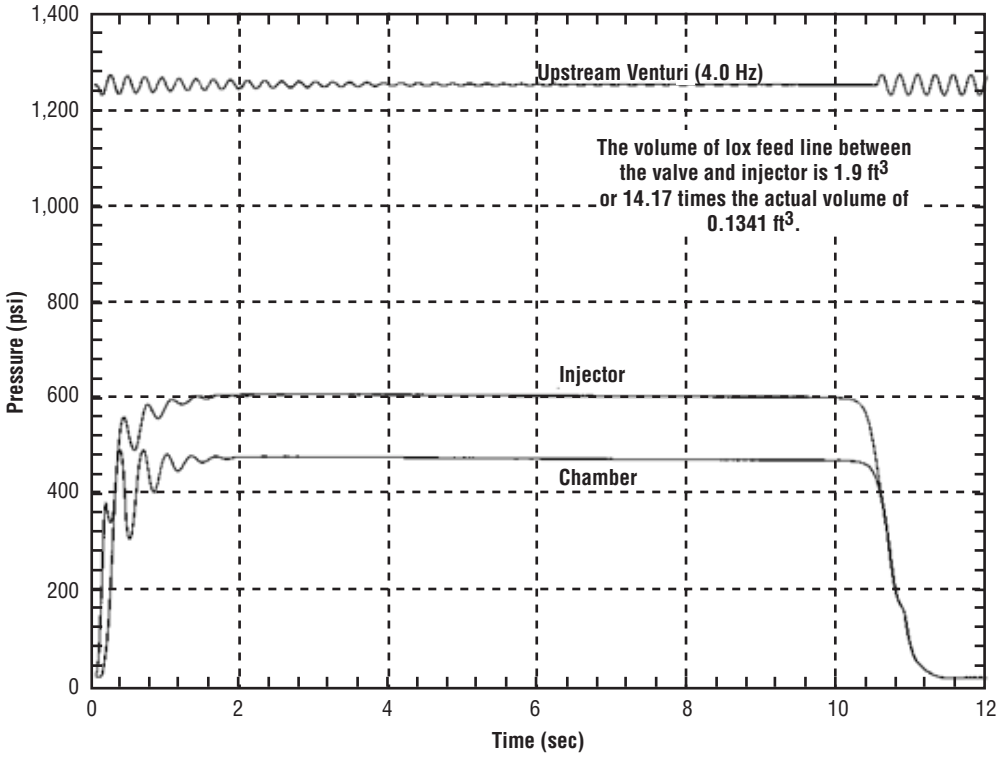

Figure 43. Simulated system pressures for test 1.

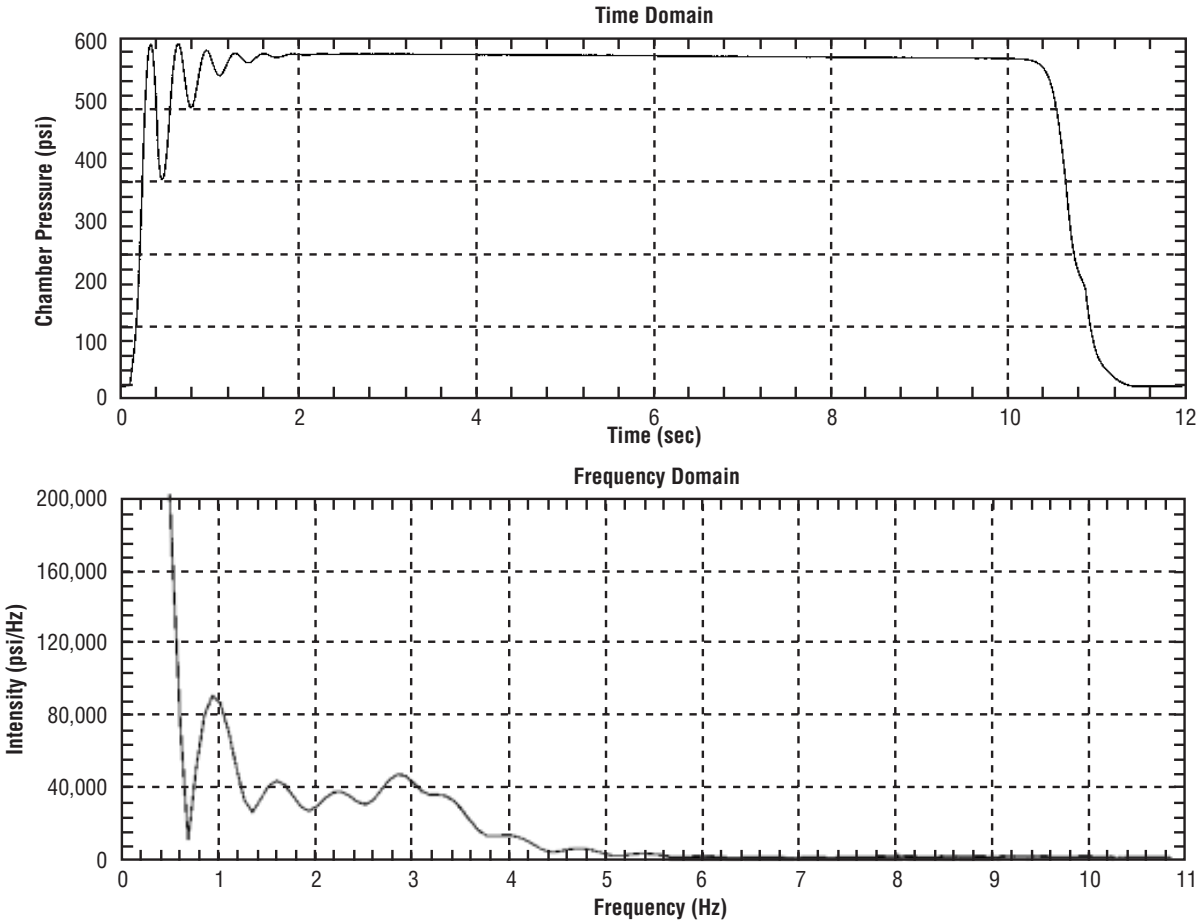

Figure 44. Simulated chamber pressure and frequency spectrum for test 1.

Test 1 was simulated third. The first attempt at simulating test 1 resulted in nonoscillatory pressures in the combustion chamber and feedsystem downstream of the venturi. Like tests 2 and 3, the feedline volume downstream of the venturi between the valve and injector was increased 14.17 times the actual value. This increase was equivalent to the actual lox compressibility being 14.17 times the compressibility as was modeled. This increase resulted in no change in the nonoscillatory pressures in the chamber and in the feedsystem downstream of the venturi. Apparently, the high impedance of the injector was effective in damping the oscillations that would have occurred due to a "soft" feedsystem.

5.4 Results of the Test 7 Simulation

Figures 45 and 46 present actual and simulated test data for test 7. Recall that test 7 was performed with a fresh fuel grain, a lox flow rate of 20 lbm/sec, the low-impedance JIRAD injector with a pressure drop of 10 percent, and an orifice immediately upstream of the injector. As in tests 1, 2, and 3, there was a very good qualitative match between the actual and simulated test data. There were minimal yet stable chamber pressure oscillations throughout the test.

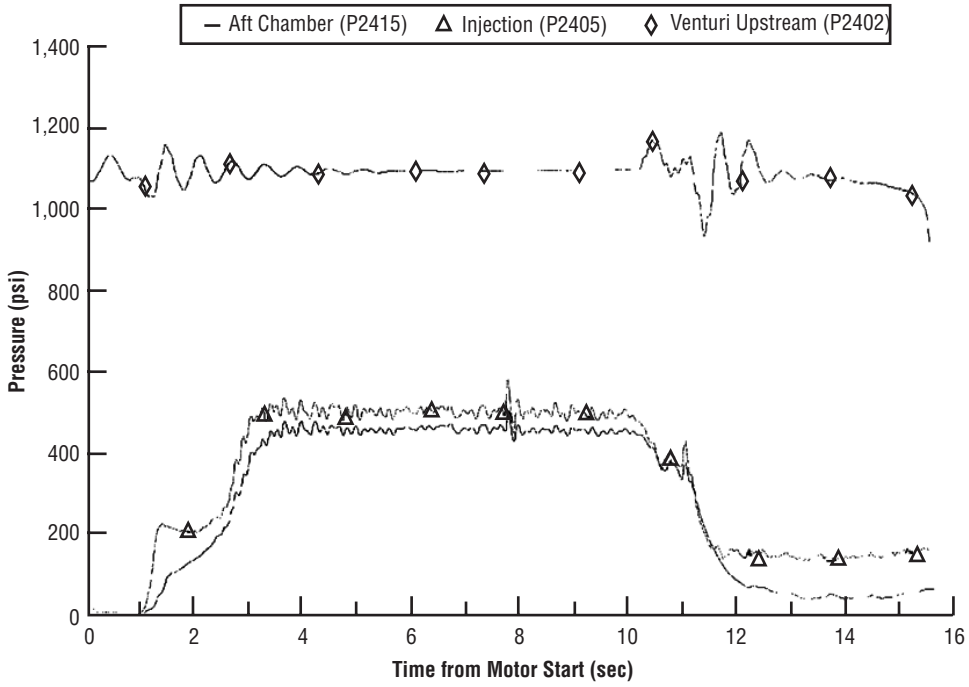

Figure 45. Actual system pressures from test 7.

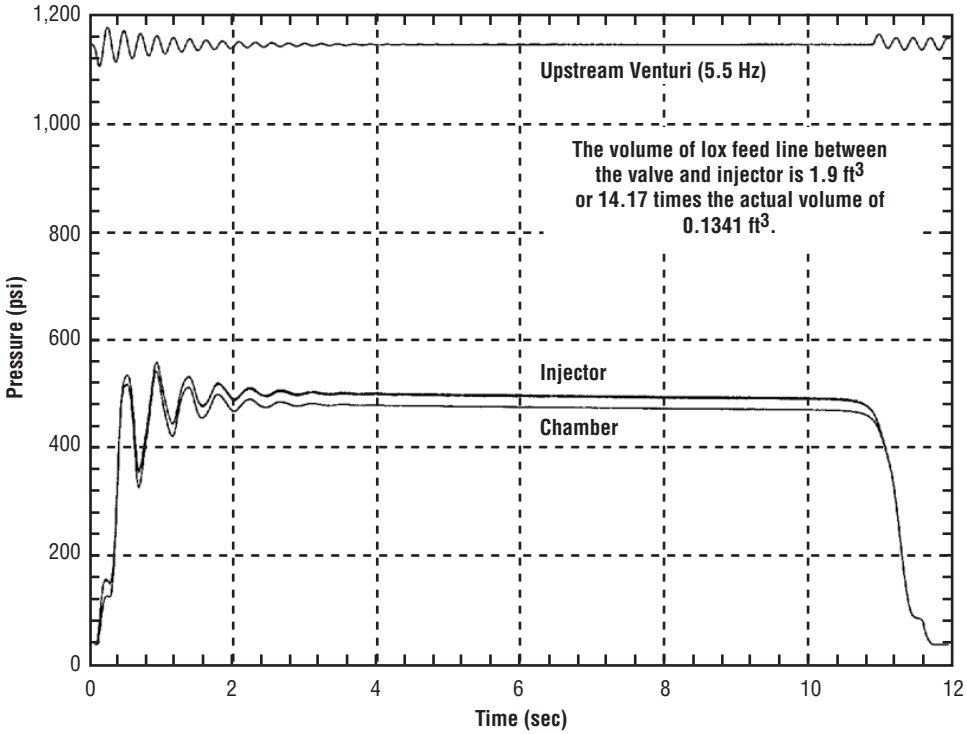

Figure 46. Simulated system pressures for test 7.

Figure 47 presents a frequency spectrum of the simulated chamber pressure. There were minor peaks and humps in the spectrum at 1.4, 2.3, and 3.3 Hz. Spectral intensity of the peaks and humps seemed to decrease with increasing frequency. These peaks and humps seemed to be associated with the mean transient of chamber pressure. Some of these same peaks and humps in the spectral intensity appeared in some degree in the spectra of tests 1, 2, and 3.

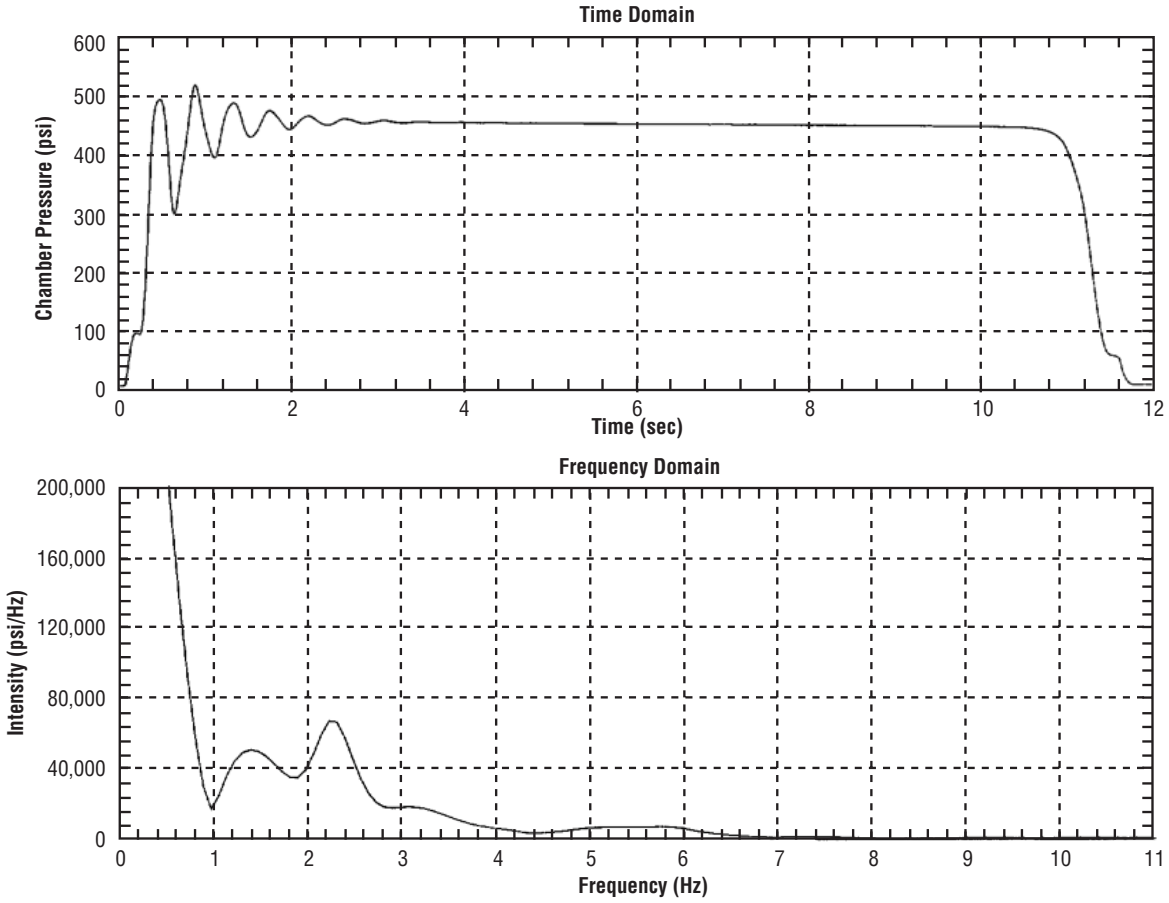

Figure 47. Simulated chamber pressure and frequency spectrum for test 7.

Test 7 was simulated last. The first attempt at simulating test 7 resulted in nonoscillatory pressures in the combustion chamber and feedsystem downstream of the venturi. Like tests 1, 2, and 3, feedline volume downstream of the venturi between the valve and injector was increased 14.17 times the actual value. This increase was equivalent to actual lox compressibility being 14.17 times the compressibility as was modeled. This increase resulted in no change in nonoscillatory pressures in the chamber and feedsystem downstream of the venturi. Apparently, the orifice increased the effective impedance of the low-impedance injector and was effective in damping the oscillations that would have occurred due to a “soft” feedsystem.

6. SUMMARY AND CONCLUSIONS

Agreement between the results of the Matrix-x transient model and actual test data was very good. This agreement between simulated and actual test data indicated that nonacoustic combustion instability in the hybrid motor was due to two causes:

- Having a lox feedsystem of excessive capacitance or insufficient stiffness was the first cause. Capacitance was defined as the product of feedline volume and liquid compressibility. Stiffness was defined as the reciprocal of capacitance. Modeling a portion of feedline with a volume 14.17 times the actual volume was the same as modeling actual compressibility as 14.17 times the compressibility as represented in the model. The large compressibility in this portion of feedline suggested presence of trapped gox. The portion of feedline in question was between the valve and injector.

- The JIRAD lox injector having had an impedance or pressure drop insufficient to provide damping against feedsystem oscillations was the second cause. However, the LSSRCS lox injector had sufficient impedance to damp feedsystem oscillations. It was also discovered that testing with a new grain of solid fuel sustained the combustion instability while testing with a used grain of solid fuel caused the combustion instability to gradually decay.

Minor peaks and humps occurred in the spectrum at 1.4, 2.3, and 3.3 Hz in the frequency spectrum of simulated chamber pressure in the case of test 7. In the case of test 1, not only were there minor peaks and humps appearing at frequencies similar to those of test 7, there were also minor peaks and humps at 0.9, 2.9, 4, and 4.7 Hz. The magnitude of spectral intensity of the peaks and humps seemed to decrease with increasing frequency. The peak at 2.3 Hz probably corresponded to the “fill/flush” frequency. Since tests 1 and 7 were stable, these peaks and humps seemed to be associated with the mean transient of chamber pressure.

There were peaks in the spectrum at 2.5, 6.4, and 10.4 Hz for tests 2 and 3 in the frequency spectrum of the simulated chamber pressure. The peak at 2.5 Hz was primary in spectral intensity in test 2, secondary in test 3, and corresponded to the “fill/flush” frequency. The peak at 6.4 Hz was slightly secondary in spectral intensity in test 2, dramatically dominant in test 3, and corresponded to the nonacoustic combustion instability associated with the lox feedline between the valve and injector. The peak at 10.4 Hz was a distant third in spectral intensity and did not correspond to any known cause. Since tests 2 and 3 were unstable, the peaks at 6.4 Hz seemed to be associated with large-amplitude oscillations in chamber pressure.

REFERENCES

1. Greiner, B.E.; and Frederick, R.A.: "Hybrid Rocket Instability," Final report: Thiokol Contract PO1175, Proposal 92–444 to the University of Alabama in Huntsville, 1992.

2. "HPTLVB (Hybrid Propulsion Technology for Launch Vehicle Boosters) Motor Testing Final Report," CD–ROM, Contract NAS8–39942, 1996.

3. Boardman, T.A.; Hawkins, D.K.; Wassom, S.R.; and Claflin, S.E.: "Nonacoustic Feedsystem Coupled Combustion Instability in Hybrid Rocket Motors," Presentation at the Hybrid Rocket Technical Committee Combustion Stability Workshop, 31st AIAA/ASME/SAE/ASEE Joint Propulsion Conference and Exhibit, 1995.

4. Carpenter, R.L.; Boardman, T.A.; Claflin, S.E.; and Harwell, R.J.: "Hybrid Propulsion Technology for Launch Vehicle Boosters: A Program Status Update," *AIAA 95–2688*, 1995.

5. Martin, C.L.: Solid and Hybrid Rocket Ballistician, NASA Marshall Space Flight Centers, Private Communication, July 1999.

6. Estey, P.N.; Altman, D.; and McFarlane, J.S.: "An Evaluation of Scaling Effects for Hybrid Rocket Motors," *AIAA 91–2517*, 1991.

7. Harrje, D.T.; and Reardon, F.H. (eds.): "Liquid Propellant Rocket Combustion Instability," *NASA SP–194*, editors: p.108, 1972.

REPORT DOCUMENTATION PAGE

Form Approved
OMB No. 0704-0188

1. AGENCY USE ONLY *(Leave Blank)*	2. REPORT DATE	3. REPORT TYPE AND DATES COVERED
	February 2000	Technical Publication

4. TITLE AND SUBTITLE
Modeling of Nonacoustic Combustion Instability in Simulations of Hybrid Motor Tests

5. FUNDING NUMBERS

6. AUTHORS
M. Rocker

7. PERFORMING ORGANIZATION NAMES(S) AND ADDRESS(ES)
George C. Marshall Space Flight Center
Marshall Space Flight Center, AL 35812

8. PERFORMING ORGANIZATION REPORT NUMBER
M–960

9. SPONSORING/MONITORING AGENCY NAME(S) AND ADDRESS(ES)
National Aeronautics and Space Administration
Washington, DC 20546–0001

10. SPONSORING/MONITORING AGENCY REPORT NUMBER
NASA/TP—2000–209905

11. SUPPLEMENTARY NOTES
Prepared for the Advanced Space Transportation Program, Space Transportation Directorate

12a. DISTRIBUTION/AVAILABILITY STATEMENT
Unclassified-Unlimited
Subject Category 20
Standard Distribution

12b. DISTRIBUTION CODE

13. ABSTRACT *(Maximum 200 words)*

A transient model of a hybrid motor was formulated to study the cause and elimination of nonacoustic combustion instability. The transient model was used to simulate four key tests out of a series of seventeen hybrid motor tests conducted by Thiokol, Rocketdyne, and Martin Marietta at NASA Marshall Space Flight Center (MSFC). These tests were performed under the Hybrid Propulsion Technology for Launch Vehicle Boosters (HPTLVB) program. The first test resulted in stable combustion. The second test resulted in large-amplitude, 6.5-Hz chamber pressure oscillations that gradually damped away by the end of the test. The third test resulted in large-amplitude, 7.5-Hz chamber pressure oscillations that were sustained throughout the test. The seventh test resulted in elimination of combustion instability with the installation of an orifice immediately upstream of the injector. Formulation and implementation of the model are the scope of this presentation.

The current model is an independent continuation of modeling presented previously by joint Thiokol–Rocketdyne collaborators Boardman, Hawkins, Wassom, and Claflin. The previous model simulated an unstable independent research and development (IR&D) hybrid motor test performed by Thiokol. There was very good agreement between the model and test data. Like the previous model, the current model was developed using Matrix-x simulation software. However, tests performed at MSFC under the HPTLVB program were actually simulated.

In the current model, the hybrid motor, consisting of the liquid oxygen (lox) injector, the multiport solid fuel grain, and nozzle, was simulated. The lox feedsystem, consisting of the tank, venturi, valve, and feed lines, was also simulated in the model. All components of the hybrid motor and lox feedsystem are treated by a lumped-parameter approach.

Agreement between the results of the transient model and actual test data was very good. This agreement between simulated and actual test data indicated that the combustion instability in the hybrid motor was due to two causes: 1. A lox feed system of insufficient stiffness, and 2. a lox injector with an impedance or pressure drop that was too low to provide damping against the feed system oscillations. Also, it was discovered that testing with a new grain of solid fuel sustained the combustion instability. However, testing with a used grain of solid fuel caused the combustion instability to gradually decay.

14. SUBJECT TERMS
spacecraft propulsion and power, combustion stability, combustion instability, nonacoustic combustion instability, hybrids, hybrid propulsion technology for launch vehicle boosters

15. NUMBER OF PAGES
60

16. PRICE CODE
A04

17. SECURITY CLASSIFICATION OF REPORT	18. SECURITY CLASSIFICATION OF THIS PAGE	19. SECURITY CLASSIFICATION OF ABSTRACT	20. LIMITATION OF ABSTRACT
Unclassified	Unclassified	Unclassified	Unlimited